Microfluidics and Nanofluidics (2025) https://doi.org/10.1007/s10404-024-02779-z

Envelope boundary conditions for the upper surface of two-dimensional canopy interacting with fluid flow

Shota Akita[1*], Kie Okabayashi[1†], and Shintaro Takeuchi[1‡]

[1] Department of Mechanical Engineering, Osaka University,
2-1 Yamada-oka, Suita, Osaka 565-0871, Japan

Abstract

Boundary conditions at the surface of a layer of flexible fibers (i.e. the canopy envelope) subjected to fluid flow are proposed for uniform and non-uniform motions of the fibers, where the fibers exhibit identical and individual motions, respectively, to understand the mechanisms of the swaying motion of the canopy. By assuming small deflections, the fibers are treated as rigid rods hinged to a flat wall and the effects of the hydrodynamic force on the fibers are expressed with the moment of fluid forces by averaging the Navier–Stokes equations. For the uniformly moving case, displacement of the envelope is represented by a mass-spring-damper system driven by the hydrodynamic force. As the non-uniformity of the canopy behavior enhances, the effects of the diffusion of fiber velocities and fluid inertia along the fiber stems play a more important role in the envelope displacement equation. Numerical simulations of fluid flow are conducted with the envelope displacement models as the boundary conditions at the canopy surface. The validity of the present models is assessed by comparison with the results of fluid-structure interaction (FSI) simulation, which directly solves the interaction between individual fibers and fluid by an immersed boundary method. With the envelope model for non-uniform displacement, the grid convergence of the numerical result is about a first order rate. The comparison of the terms in the envelope model for non-uniform displacement shows that diffusion of fiber velocities dominates the motion of fibers. The applicability of the model is assessed by varying the number density of the fibers.

Keywords

Canopy-tip boundary condition, Envelope model, Coarse graining, Fluid structure interaction

* akita@fluid.mech.eng.osaka-u.ac.jp, u953355h@ecs.osaka-u.ac.jp
† ORCID ID: 0000-0001-9682-647X
‡ ORCID ID: 0000-0003-0091-4542

1 Introduction

The interaction problem between a fluid and a layer of fibers anchored at one end to a wall is observed in many engineering applications, in biology and in the natural environment. The layer of fibers is commonly referred to as a canopy, and the function of canopies has been studied extensively because of its importance in the transport phenomena of mass, momentum and energy. For example, the collective motions of cilia facilitate the transport of viscous liquids (Fulford and Blake 1986), which is known to protect against several diseases on the cell surface of the lung (Tilley et al. 2015). For some micro-organisms in water, the metachronal wave patterns are known to effectively move the fluid around them (Elgeti and Gompper 2013; Chateau et al. 2017; Zhang et al. 2021) and eventually propel themselves. Metachronal waves have also been applied to microfluidic devices (Wang et al. 2022; Oosten et al. 2009; Vilfan et al. 2010; Khaderi et al. 2015; Milana et al. 2020). A typical example is an array of artificial cilia installed on a wall manipulated by electronic signals to generate micro-flow patterns (Wang et al. 2022). Most of the above applications are in a low Reynolds number range, whereas the effects of high Reynolds numbers give rise to different flow aspects such as the interaction between the turbulent flow and the canopy. Turbulent flows above the canopy are known to have such organized eddy structures as spanwise "rolls" and streamwise "ribs" (Gao et al. 1989; Kanda et al. 1994; Finnigan 2000). These structures consist of the strong flow entering the canopy (sweep) and the weak flow leaving it (ejection). Many researchers have shown that the sweep motion dominantly transfers the momentum of the fluid (Finnigan 1978; Raupach et al. 1986; Kanda et al. 1994), and, in turn, promotes heat transfer (Finnigan 2000; Boppana et al. 2014; Li et al. 2018). Although there are a variety of phenomena and functions associated with canopy flows over a wide range of Reynolds numbers, to understand the fundamental mechanisms of fluid flows induced by canopy motion (and the induced motion of the canopy by the external flow), in the present study we focus on the problem of fluid-fiber interaction in a laminar region.

A number of mathematical models have been developed and numerical simulations have been conducted. Solving for the motion of individual fibers and the fluid flow around them can give an accurate picture of the interaction problem (Stoesser et al. 2009; Mattis et al. 2015; Chen and Zou 2019). However, it is computationally intensive as the number of fibers increases, as at least a few grid points are required in each inter-fiber region to resolve the fluid-fiber interaction. This computational

cost can be reduced by including the effect of the canopy as inertial and/or external force terms in the governing equations of the fluid (Monti 2020; Nepf 2012; Zhang and Su 2008). There are also efforts to model canopies as specialized materials. Secomb et al. (1998) modeled the glycocalyx on the endothelial wall as a layer of compressible material in his simulations of blood flow. Gopinath and Mahadevan (2011) formulated an elastohydrodynamic model that treats the vegetation layer as a porous bed. The above mathematical models are valuable for large-scale analysis of canopy flow with less computational cost. However, as the models do not reflect the motions and properties of individual fibers, they do not provide pictures relevant to the fluid-fiber interaction, such as the propagation of oscillatory fiber motion, taking into account the underlying physics of canopy motion.

On the other hand, in the field of micro-organisms, models that replicate the surface of the canopy have been studied. The pioneering study by Lighthill (1952) is called the squirmer model. In his theory, the flow fields were described with the polar coordinates and the surface of the ciliay layer was treated with Dirichlet conditions for the velocity components. Since then, squirmer models have been extensively studied by many researchers. Blake (1971) considered the surface deformation, and after his study, the upper surface of the canopy is commonly referred to as the "envelope". Khair and Chisholm (2014) introduced the higher-order velocity components by asymptotic expansion in the Stokes flow regime, and Wang and Ardekani (2012) studied analytically the effect of convective inertia on the squirmer. Although these ideas are insightful, the velocities at the canopy surface are prescribed and the behavior of individual cilia is not taken into account. There have also been studies focusing on the mechanism of ordered behavior in an array of cilia (Uchida and Golestanian 2010; Meng et al. 2021), and their phase model revealed dispersion relations of synchronized oscillations. However, there may be situations where strong interaction between flow and individual fibers induces non-uniformity of fiber motions, and the mechanism for the development of asynchronous motions may not be explained.

In the present study, new fluid boundary conditions at the canopy surface are developed to reveal the fundamental mechanisms of canopy flow by considering individual fiber motions and fluid-fiber interactions, and the models are applied to numerical simulations to assess the validity. In the modeling process, the motions of the fluid and fibers inside the canopy are coarse-grained and reflected onto the envelope of the fiber tips, so that only the fluid motion above the canopy is solved

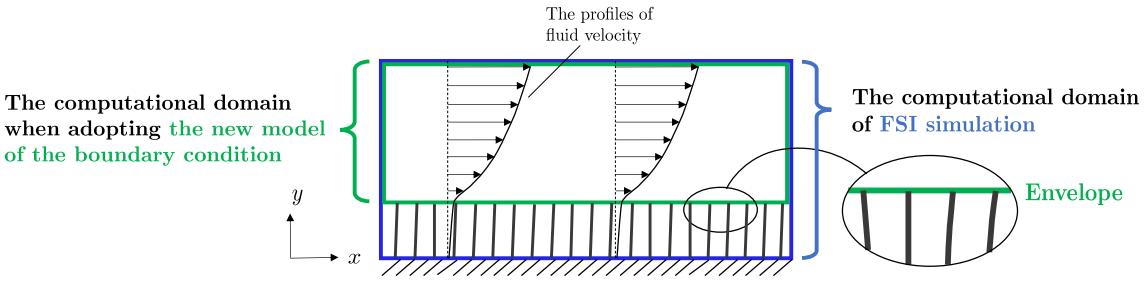

Figure 1: Schematic of the computational domain. With the boundary conditions of the velocity and pressure gradient obtained by our envelope model, only the fluid motion above the canopy (shown in green) is solved, whereas the fluid motion in the whole fluid region (shown in blue) and the deformations of individual fibers need to be solved for fluid-structure interaction (FSI) simulation.

with a smaller computational domain (see Fig. 1). To demonstrate the basic idea of our envelope models, we restrict the modeling mainly to two dimensions, and by assuming small tip displacements, the fibers are treated as rigid rods and the effect of bending stress is modeled with torsion spring. By considering a reduced-order fluid-fiber interaction at a relatively small inter-fiber spacing with explicit mechanical properties of the fibers, the tip displacements of the fibers are represented as a time-evolving envelope for the overlying fluid without explicitly solving the individual fiber motions.

The structure of this paper is as follows. After the problem statement in Sec. 2, the governing equations for the fiber and the fluid are summarized in Secs. 3 and 4, respectively. The envelope models are developed separately for uniform and non-uniform motions of fibers in Secs. 5 and 6, respectively. The numerical methods are explained in Sec. 7. The models are validated in Sec. 8 by comparing the results with those obtained by fluid-structure interaction (FSI) simulation including individual fibers. Finally, Sec. 9 concludes the study.

2 Problem statement

We consider uniform (synchronous) and non-uniform (asynchronous/individual) motions of fibers induced by fluid flow above and inside a layer of fibers (canopy), and develop envelope models for fiber tip displacement.

Throughout the present study, the fibers are arranged at uniform intervals (a) along the x axis. The wall-normal direction is the y axis. To construct envelope models for tip displacement, we make the following assumptions:

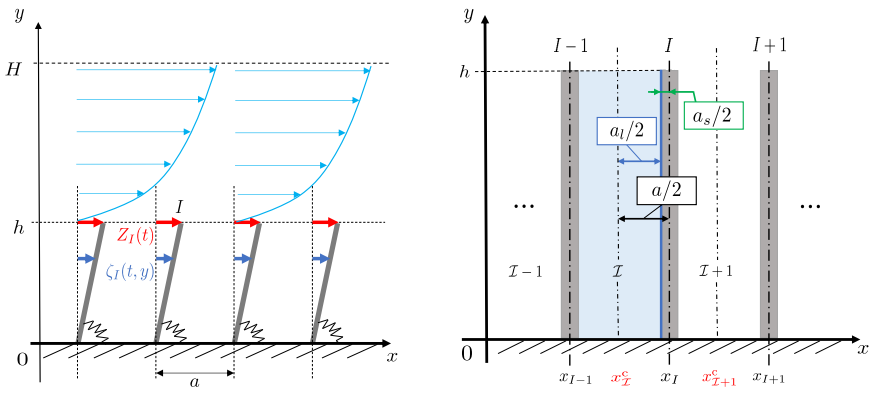

Figure 2: Schematic of rigid fibers hinged to a flat wall. The x component of the displacement of the I-th fiber is $\zeta_I(t, y)$, and the tip displacement of the fiber is specifically denoted as $Z_I(t)$. The fibers are placed at a constant interval a which consists of the fiber thickness a_s and the length of the fluid-filled region (fluid film thickness) a_l; $a = a_s + a_l$. The fibers and fluid-filled regions are labeled with the indices $I, I \pm 1, \cdots$ and $\mathcal{I}, \mathcal{I} \pm 1, \cdots$, respectively.

1. Displacements of the fibers are sufficiently small.
2. Fibers are simplified to rigid rods hinged to a flat wall, as schematically shown in Fig. 2(a), and neutral angle of the fibers is set to $\pi/2$ with respect to the x axis. Effect of bending stress is modeled with torsion spring.
3. Fluid film thickness (i.e., surface-to-surface distance of neighboring fibers) a_l and fiber length h (see Fig. 2(b)) satisfy the following relations: $a_l/h \lesssim 1$ and $(a_l/h)^2 \ll 1$.
4. The fluid motion between neighboring two fibers is diffusion-dominated.

Based on the above assumptions, the equations of motion for the fiber(s) and fluid are summarized in Secs. 3 and 4, respectively, and then, followed by specific modelings for uniform and non-uniform motions of the canopy in Secs. 5 and 6, respectively.

Hereafter, the fibers are labeled with the indices $I, I \pm 1, \cdots$, and the neighboring fluid-filled regions are labeled with the indices $\mathcal{I}, \mathcal{I} \pm 1, \cdots$, as illustrated in Fig. 2(b). The x coordinate of the center of the fluid region $\mathcal{I}$ is denoted as $x_{\mathcal{I}}^{\mathrm{c}}$, and the x coordinate of the base of the fiber I is denoted x_I.

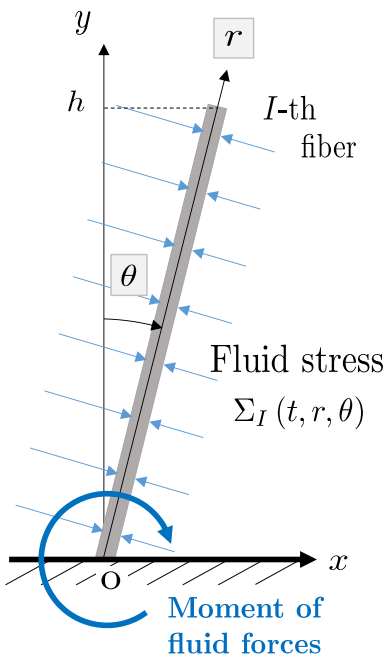

Figure 3: Local coordinates for a fiber, r and θ, and the positive direction of the first-order moment of the fluid force.

3 Governing equation of a tip of fiber

By taking the moment of the forces on the fiber around $(x, y) = (x_I, 0)$ in the clockwise direction as illustrated in Fig. 3, the conservation of angular momentum is given as follows:

$$\int_0^h r\rho_s \frac{\partial^2 (r\theta)}{\partial t^2} a_s \mathrm{d}r = -k\theta + \int_0^h r\Sigma_I(t, r, \theta)\mathrm{d}r \ , \tag{1}$$

where t is the time, r is the distance measured from $(x, y) = (x_I, 0)$, ρ_s is the density of the fiber, a_s is the width of the fiber, k is the spring constant per angle θ measured from the y axis, and $\Sigma_I(t, r, \theta)$ is the fluid stress acting on the I-th fiber (see Fig. 3).

By introducing $\cos\theta \sim 1$ and $\theta \sim \sin\theta = Z_I/h$ (Assumption 1) with $Z_I(t)$ as the horizontal displacement of the I-th fiber at the free end, Eq. (1) is written in a form that only depends on t and y:

$$\frac{1}{3}\rho_s a_s h^2 \frac{\mathrm{d}^2 Z_I}{\mathrm{d}t^2} = -\frac{k}{h} Z_I + \int_0^h y\Sigma_I(t, y, Z_I)\mathrm{d}y \ . \tag{2}$$

To determine the value of the spring constant k, we use a free vibration of a fiber. By excluding the effect of surrounding fluid, Eq. (2) is simplified as follows:

$$\frac{1}{3}\rho_s a_s h^2 \frac{\mathrm{d}^2 Z_I}{\mathrm{d}t^2} = -\frac{k}{h} Z_I. \tag{3}$$

The harmonic frequency $\omega_{\rm fv} = \sqrt{(k/h)/(\rho_s a_s h^2/3)}$, is also described by the vibration theory of a cantilever of bending stiffness EI (with the Young's modulus E and moment of inertia I) and the cross-sectional area A_s, as

$$\omega_{\rm fv} = \sqrt{\frac{EI}{\rho_s A_s}} \frac{\lambda_1^2}{h^2} \ , \tag{4}$$

where λ_i is a constant that depends on vibration modes, and the first vibration mode is identified as $\lambda_1 \coloneqq 1.87$. Then, Eq. (2) takes the following form:

$$\frac{1}{3}\rho_s a_s h^2 \frac{{\rm d}^2 Z_I}{{\rm d}t^2} = -\frac{\lambda_1^4}{3}\frac{EI}{A_s}\frac{a_s}{h^2} Z_I + R\int_0^h y \Sigma_I(t, y, Z_I){\rm d}y \ , \tag{5}$$

where a correction factor R is newly introduced to consider the induced effect of the surrounding fluid.

The fluid stress acting on the I-th fiber $\Sigma_I(t, y, Z_I)$ is given as follows:

$$\begin{aligned} \Sigma_I(t, y, Z_I) = &- T_{xx}|_{x=x_I^{\rm c}+a_l/2} + T_{xx}|_{x=x_{I+1}^{\rm c}-a_l/2} \\ &+ \tau_{sI}\ a_s \delta(y-h), \end{aligned} \tag{6}$$

where T_{xx} is the hydrodynamic stress given later, τ_{sI} is the shear stress at the tip of rigid fiber, and δ is the Dirac delta function.

4 Governing equations for fluid motion

The fluid is assumed to be incompressible Newtonian fluid of constant density ρ_l. The governing equations are the equation of continuity and the Navier–Stokes equations:

$$\frac{\partial u}{\partial x} + \frac{\partial v}{\partial y} = 0 \ , \tag{7a}$$

$$\frac{\partial u}{\partial t} + u\frac{\partial u}{\partial x} + v\frac{\partial u}{\partial y} = -\frac{1}{\rho_l}\frac{\partial p}{\partial x} + \nu\left(\frac{\partial^2 u}{\partial x^2} + \frac{\partial^2 u}{\partial y^2}\right) - \frac{1}{\rho_l}\frac{\Delta p}{\Delta x} \ , \tag{7b}$$

$$\frac{\partial v}{\partial t} + u\frac{\partial v}{\partial x} + v\frac{\partial v}{\partial y} = -\frac{1}{\rho_l}\frac{\partial p}{\partial y} + \nu\left(\frac{\partial^2 v}{\partial x^2} + \frac{\partial^2 v}{\partial y^2}\right) \ , \tag{7c}$$

where u and v are the velocity components in the x and y directions, respectively, p is the pressure, $\Delta p/\Delta x$ is the externally-induced pressure gradient (employed in Sec. 5), and ν is the kinetic viscosity of the fluid.

To establish the model for Σ_I, we evaluate the orders of magnitudes of the variables in Eq. (7) as $O[x] = a_l$, $O[y] = h$, $O[u] = U$, $O[v] = V$. From the equation of continuity, the magnitudes of the velocities U and V are related as $U = \epsilon V$, where $\epsilon = a_l/h$ is the aspect ratio of the fluid-filled region between neighboring fibers. By introducing the Reynolds number as $Re = Uh/\nu$, the magnitudes of the terms are evaluated as follows:

$$\epsilon\, O\left[u\frac{\partial u}{\partial x}\right] = \epsilon\, O\left[v\frac{\partial u}{\partial y}\right] = \epsilon^2 Re\, O\left[\nu\frac{\partial^2 u}{\partial x^2}\right] \quad \left(= \frac{U^2}{h}\right) , \tag{8a}$$

$$\epsilon\, O\left[u\frac{\partial v}{\partial x}\right] = \epsilon\, O\left[v\frac{\partial v}{\partial y}\right] = \epsilon^2 Re\, O\left[\nu\frac{\partial^2 v}{\partial x^2}\right] \quad \left(= \frac{U^2}{a_l}\right) . \tag{8b}$$

Note that the order of magnitude of $\partial^2 u/\partial y^2$ cannot be determined in advance, as u can vary strongly along y near the canopy surface, which will be mentioned in Sec. 8.2. Therefore, staring from Assumption 3 ($\epsilon \lesssim 1$ and $\epsilon^2 \ll 1$) and further assuming $\epsilon^2 Re \ll 1$ (i.e. Assumption 4), Eqs. (7b) and (7c) are simplified as follows:

$$\frac{\partial u}{\partial t} = -\frac{1}{\rho_l}\frac{\partial p}{\partial x} + \nu\left(\frac{\partial^2 u}{\partial x^2} + \frac{\partial^2 u}{\partial y^2}\right) - \frac{1}{\rho_l}\frac{\Delta p}{\Delta x} , \tag{9a}$$

$$\frac{\partial v}{\partial t} = -\frac{1}{\rho_l}\frac{\partial p}{\partial y} + \nu\frac{\partial^2 v}{\partial x^2} . \tag{9b}$$

For the convenience in the following sections, we introduce

$$T_{xx} = -\left(p + \frac{\Delta p}{\Delta x}x\right) + 2\mu\frac{\partial u}{\partial x} , \tag{10}$$

where μ ($= \nu/\rho_l$) is the viscous coefficient. Eq. (9a) is simplified to the following form:

$$\rho_l\frac{\partial u}{\partial t} = \frac{\partial T_{xx}}{\partial x} + \mu\frac{\partial^2 v}{\partial x \partial y} + \mu\frac{\partial^2 u}{\partial y^2} . \tag{11}$$

5 Envelope model for uniform motion of fibers

In this section, we consider the uniform motion of fibers induced by a constant pressure gradient, $-\Delta p/\Delta x$. In this situation, the fluid stress distributions are the same in each fluid-filled region ($^\forall\mathcal{I}$) and on each fiber surface ($^\forall I$). Therefore, in this section, $Z_I(t)$ and $\Sigma_I(t, y)$ are simply denoted as $Z(t)$ and $\Sigma(t, y)$, respectively.

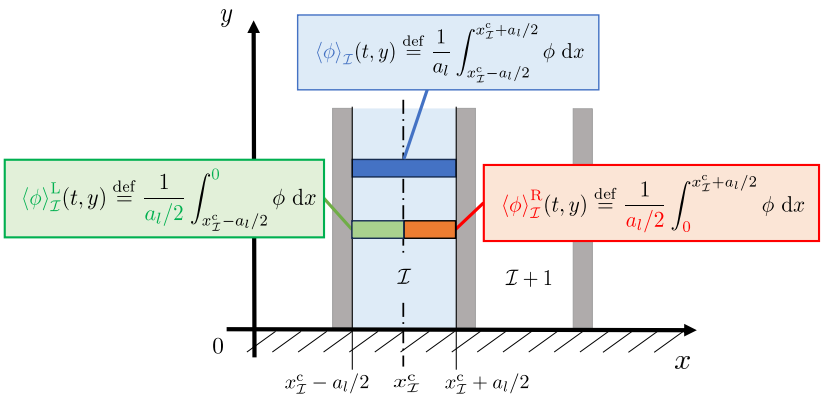

Figure 4: Schematic of three averages of a fluid variable ϕ at the level of y; $\langle\phi\rangle_{\mathcal{I}}^{\mathrm{L}}$, $\langle\phi\rangle_{\mathcal{I}}^{\mathrm{R}}$, and $\langle\phi\rangle_{\mathcal{I}}$ are referred to as left, right, and total average, respectively.

In the following, a time-dependent equation for Z is derived by modeling Σ. We introduce the following piecewise averages in the fluid region $\mathcal{I}$ for a fluid variable $\phi(t,x,y)$:

$$\text{Left ave.} \quad : \quad \langle\phi\rangle_{\mathcal{I}}^{\mathrm{L}} \overset{\text{def}}{=} \frac{1}{a_l/2}\int_{x_{\mathcal{I}}^{\mathrm{c}}-a_l/2}^{x_{\mathcal{I}}^{\mathrm{c}}} \phi(t,x,y)\,\mathrm{d}x\ , \tag{12a}$$

$$\text{Total ave.} \quad : \quad \langle\phi\rangle_{\mathcal{I}} \overset{\text{def}}{=} \frac{1}{a_l}\int_{x_{\mathcal{I}}^{\mathrm{c}}-a_l/2}^{x_{\mathcal{I}}^{\mathrm{c}}+a_l/2} \phi(t,x,y)\,\mathrm{d}x\ , \tag{12b}$$

$$\text{Right ave.} \quad : \quad \langle\phi\rangle_{\mathcal{I}}^{\mathrm{R}} \overset{\text{def}}{=} \frac{1}{a_l/2}\int_{x_{\mathcal{I}}^{\mathrm{c}}}^{x_{\mathcal{I}}^{\mathrm{c}}+a_l/2} \phi(t,x,y)\,\mathrm{d}x\ , \tag{12c}$$

as schematically shown in Fig. 4. Eqs. (12a) and (12c) are used in Sec. 6.

5.1 Velocity in the y direction at envelope

To develop boundary conditions for the fluid flow at the free end of the canopy, we start with the y component of the fluid velocity v. From Assumption 1 and the uniform motion condition, the volume variation of each fluid region in the canopy is reasonably assumed to be negligible. Therefore, in the $\mathcal{I}$-th fluid region, the inflow volume per unit time $\dot{Q}_{\mathcal{I}}$ $(= -a_l \langle v\rangle_{\mathcal{I}})$ over the cross section at y can be regarded as follows:

$$\dot{Q}_{\mathcal{I}}(t,y) \sim 0\ , \tag{13}$$

which yields $\langle v\rangle_{\mathcal{I}} = 0$. From Assumptions 1 and 3, the envelope boundary condition of v is given as follows:

$$v(t,x,y) = 0\ , \tag{14}$$

and therefore, $\partial v/\partial y|_{x=x_{\mathcal{I}}^{\mathrm{c}}\pm a_l/2}$ is treated as 0 in the following.

5.2 Motion of canopy surface in the x direction

Eq. (11) is integrated with respect to x in the range between $x_{\mathcal{I}}^{\mathrm{c}} \mp a_l/2$, and the following equation is obtained:

$$\rho_l a_l \frac{\partial \langle u \rangle_{\mathcal{I}}}{\partial t} = \left[T_{xx} \right]_{x_{\mathcal{I}}^{\mathrm{c}} - a_l/2}^{x_{\mathcal{I}}^{\mathrm{c}} + a_l/2} + \mu a_l \left\langle \frac{\partial^2 u}{\partial y^2} \right\rangle_{\mathcal{I}} . \tag{15}$$

Considering the following similarity of the fluid stresses in the neighboring regions ($\mathcal{I}$ and $\mathcal{I}+1$):

$$T_{xx}|_{x=x_{\mathcal{I}+1}^{\mathrm{c}} - a_l/2} = T_{xx}|_{x=x_{\mathcal{I}}^{\mathrm{c}} - a_l/2} - \frac{\Delta p}{\Delta x} a ,$$

where $a = a_s + a_l$, the fluid stress Σ (Eq. (6)) is rearranged as follows:

$$\Sigma(t, y) = - \left[T_{xx} \right]_{x=x_{\mathcal{I}}^{\mathrm{c}} - a_l/2}^{x=x_{\mathcal{I}}^{\mathrm{c}} + a_l/2} - \frac{\Delta p}{\Delta x} a + \tau_{sI} \ a_s \delta(y - h) . \tag{16}$$

By substituting Eq. (15) into Eq. (16) and integrating by parts, the moment of fluid force (Eq. (2)) is obtained as follows:

$$\begin{aligned} \int_0^h \Sigma \ y \mathrm{d}y = & - \rho_l a_l \int_0^h \frac{\partial \langle u \rangle}{\partial t} y \mathrm{d}y \\ & - \mu a_l \langle u \rangle |_{y=h} + \tau a h - \frac{a h^2}{2} \frac{\Delta p}{\Delta x} . \end{aligned} \tag{17}$$

Here, by denoting the shear stress on the upper boundary as $\tau_l = \mu \langle \partial u / \partial y \rangle |_{y=h}$, the shear stress on the surface of canopy τ is introduced as follows:

$$\tau a = \tau_l a_l + \tau_s a_s . \tag{18}$$

In Eq. (17), the indices $\mathcal{I}$ and I for $\langle u \rangle$ and τ are omitted because they are identical for each inter-fiber region.

From the narrow gap assumption (Assumption 3), we approximate $\langle u \rangle$ with the x component of the fiber velocity $\partial \zeta / \partial t$ as follows:

$$\langle u \rangle \sim \frac{\partial \zeta}{\partial t} = \frac{y}{h} \frac{\mathrm{d}Z}{\mathrm{d}t} . \tag{19}$$

We consider that Eq. (19) becomes more reliable as the Reynolds number and the unsteadiness are smaller and weaker, respectively.

Substitution of Eq. (19) into Eq. (17) yields the following equation:

$$\int_0^h \Sigma \ y \mathrm{d}y = -\frac{1}{3} \rho_l a_l h^2 \frac{\mathrm{d}^2 Z}{\mathrm{d}t^2} - \mu a_l \frac{\mathrm{d}Z}{\mathrm{d}t} + \tau a h - \frac{1}{2} a h^2 \frac{\Delta p}{\Delta x} , \tag{20}$$

and using the above equation for Eq. (5), the time development of the tip displacement Z for the uniform deformation case is obtained as follows:

$$\frac{\widetilde{\rho}h^2}{3}\frac{\mathrm{d}^2 Z}{\mathrm{d}t^2} = -RC\frac{\mathrm{d}Z}{\mathrm{d}t} - \frac{\lambda_1^4}{3}\frac{EI}{A_s h^2}\frac{a_s}{a}Z - \frac{R}{2}\frac{\Delta p}{\Delta x}h^2 + R\tau h \ , \tag{21}$$

where $\widetilde{\rho} \stackrel{\mathrm{def}}{=} \rho_s\varphi_s + R\rho_l\varphi_l$, $\varphi_k \stackrel{\mathrm{def}}{=} a_k/a$ $(k = s, l)$ is the volume ratio of the region occupied by the fiber or fluid, and the damping coefficient $\mu_l a_l/a$ is modified as $C(Re^{-1})$ to cover a wider flow condition. After solving the above equation, $\langle u\rangle$ is obtained by Eq. (19), and $\langle u\rangle|_{y=h}$ acts as a boundary condition on the envelope for the fluid flow above it, which completes the coarse-graining process in the canopy region.

5.3 Pressure gradient in the y direction at envelope

We determine the boundary condition for $\partial p/\partial y$ at the envelope from $\langle \partial p/\partial y\rangle$. From Eq. (9b), $\langle \partial p/\partial y\rangle$ is obtained as follows:

$$\left\langle \frac{\partial p}{\partial y} \right\rangle\bigg|_{y=h} = \mu \left\langle \frac{\partial^2 v}{\partial x^2} \right\rangle\bigg|_{y=h} - \rho_l \left\langle \frac{\partial v}{\partial t} \right\rangle\bigg|_{y=h} \sim 0 \ . \tag{22}$$

Hereafter, Eqs. (22), (14), and (19) associated with the envelope displacement equation (21) are referred to as "envelope boundary conditions" or simply "envelope model".

6 Envelope model for non-uniform motion of fibers

In this section, we extend the envelope model of Sec. 5 to allow the fibers to move independently. The non-uniformity of the fiber deformations is induced by the local fluid force, and therefore, the pressure gradient $(\Delta p/\Delta x)$ in the previous section is eliminated for this purpose.

The mathematical models for the fluid velocities in the y and x directions at the canopy surface are explained in Secs. 6.1 and 6.2, respectively, and the pressure gradient is modeled in Sec. 6.3.

6.1 Velocity in the y direction at envelope

When two fibers move towards or away from each other in a stationary fluid, the fluid moves out of or into the inter-fiber region across the envelope, respectively. In the $\mathcal{I}$-th fluid region, the inflow

per unit time $\dot{Q}_{\mathcal{I}}$ at y gives the following relation:

$$\dot{Q}_{\mathcal{I}}(t,y) \sim \frac{1}{2}\left(\frac{\partial \zeta_I}{\partial t} - \frac{\partial \zeta_{I-1}}{\partial t}\right) y = \frac{1}{2h}\left(\frac{\mathrm{d}Z_I}{\mathrm{d}t} - \frac{\mathrm{d}Z_{I-1}}{\mathrm{d}t}\right) y^2 \ , \tag{23}$$

and, the average of v at the same level is given as follows:

$$\langle v \rangle_{\mathcal{I}}(t,y) = -\frac{\dot{Q}_{\mathcal{I}}}{a_l} = -\frac{1}{2a_l h}\left(\frac{\mathrm{d}Z_I}{\mathrm{d}t} - \frac{\mathrm{d}Z_{I-1}}{\mathrm{d}t}\right) y^2 \ . \tag{24}$$

From the diffusion-dominated assumption (Assumption 4), we assume a laminar velocity profile for $v(t,x,y)$. From the boundary condition $v \sim 0$ at the fiber surfaces ($x = x^{\mathrm{c}}_{\mathcal{I}} \pm a_l/2$), the following quadratic function of x is obtained in each fluid region:

$$v(t,x,y) = (v_0)_{\mathcal{I}}\left[(x - x^{\mathrm{c}}_{\mathcal{I}})^2 - \frac{a_l^2}{4}\right] \qquad (|x - x^{\mathrm{c}}_{\mathcal{I}}| \le a_l/2) \ , \tag{25}$$

where $(v_0)_{\mathcal{I}}$ is a function of t and y. Substituting Eq. (25) into Eq. (24), $(v_0)_{\mathcal{I}}$ is identified and v is finally obtained as follows:

$$v(t,x,y) = \frac{3}{a_l^3 h}\left(\frac{\mathrm{d}Z_I}{\mathrm{d}t} - \frac{\mathrm{d}Z_{I-1}}{\mathrm{d}t}\right)\left[(x - x^{\mathrm{c}}_{\mathcal{I}})^2 - \frac{a_l^2}{4}\right] y^2 \qquad (|x - x^{\mathrm{c}}_{\mathcal{I}}| \le a_l/2) \ . \tag{26}$$

In particular, at the envelope ($y = h$) in the $\mathcal{I}$-th fluid region, the velocity is expressed as follows:

$$v|_{y=h} = \frac{3h}{a_l^3}\left(\frac{\mathrm{d}Z_I}{\mathrm{d}t} - \frac{\mathrm{d}Z_{I-1}}{\mathrm{d}t}\right)\left[(x - x^{\mathrm{c}}_{\mathcal{I}})^2 - \frac{a_l^2}{4}\right] \qquad (|x - x^{\mathrm{c}}_{\mathcal{I}}| \le a_l/2) \ . \tag{27}$$

6.2 Motion of canopy surface in the x direction

In the $\mathcal{I}$-th fluid region, Eq. (11) is integrated in the range of $[x^{\mathrm{c}}_{\mathcal{I}}, x]$:

$$\rho_l \int_{x^{\mathrm{c}}_{\mathcal{I}}}^{x} \frac{\partial u}{\partial t}\mathrm{d}x = [T_{xx}]_{x=x^{\mathrm{c}}_{\mathcal{I}}}^{x=x} + \mu\left[\frac{\partial v}{\partial y}\right]_{x=x^{\mathrm{c}}_{\mathcal{I}}}^{x=x} + \mu \int_{x^{\mathrm{c}}_{\mathcal{I}}}^{x} \frac{\partial^2 u}{\partial y^2}\mathrm{d}x \ . \tag{28}$$

By substituting Eq. (28) into Eq. (6), the fluid stress acting on the I-th fiber is obtained with the left- and right-averages of u (see Eqs. (12a) and (12c)) as follows:

$$\begin{aligned}\Sigma_I(t,y,Z_I) = &-\frac{\rho_l a_l}{2}\frac{\partial\left(\langle u\rangle^{\mathrm{R}}_{\mathcal{I}} + \langle u\rangle^{\mathrm{L}}_{\mathcal{I}+1}\right)}{\partial t} + \frac{\mu a_l}{2}\frac{\partial^2\left(\langle u\rangle^{\mathrm{R}}_{\mathcal{I}} + \langle u\rangle^{\mathrm{L}}_{\mathcal{I}+1}\right)}{\partial y^2} \\ &- \left[p + \mu\frac{\partial v}{\partial y}\right]_{x=x^{\mathrm{c}}_{\mathcal{I}}}^{x=x^{\mathrm{c}}_{\mathcal{I}+1}} + \tau_{sI}\ a_s\delta(y-h) \ .\end{aligned} \tag{29}$$

To evaluate the third term in the right-hand side (RHS) of Eq. (29), Eq. (9b) is integrated in the range between y and h as follows:

$$\rho_l \int_y^h \frac{\partial v}{\partial t} \mathrm{d}y = [-p]_{y=y}^{y=h} + \mu \int_y^h \frac{\partial^2 v}{\partial x^2} \mathrm{d}y \ , \tag{30}$$

which is modified to fit the form of Eq. (29) as follows:

$$\left(p + \mu \frac{\partial v}{\partial y} \right) \Big|_{y=y} = \mu \left. \frac{\partial v}{\partial y} \right|_{y=y} + p|_{y=h} - \int_h^y \left[\rho_l \frac{\partial v}{\partial t} - \mu \frac{\partial^2 v}{\partial x^2} \right] \mathrm{d}y \ . \tag{31}$$

By substituting Eq. (31) into Eq. (29), the moment of fluid forces is obtained as follows:

$$\begin{aligned} \int_0^h \Sigma_I y \mathrm{d}y = & - \frac{\rho_l a_l}{2} \int_0^h \left(\frac{\partial \langle u \rangle_{\mathcal{I}}^{\mathrm{R}}}{\partial t} + \frac{\partial \langle u \rangle_{\mathcal{I}+1}^{\mathrm{L}}}{\partial t} \right) y \mathrm{d}y \\ & + \frac{\mu a_l}{2} \int_0^h \left(\frac{\partial^2 \langle u \rangle_{\mathcal{I}}^{\mathrm{R}}}{\partial y^2} + \frac{\partial^2 \langle u \rangle_{\mathcal{I}+1}^{\mathrm{L}}}{\partial y^2} \right) y \mathrm{d}y \\ & - \frac{1}{2} [p|_{y=h}]_{x=x_{\mathcal{I}}^{\mathrm{c}}}^{x=x_{\mathcal{I}+1}^{\mathrm{c}}} h^2 + \tau_{sI} \ a_s h + \Gamma_I, \end{aligned} \tag{32}$$

where

$$\begin{aligned} \Gamma_I = & \left[-\mu h v|_{y=h} + \mu \int_0^h v \mathrm{d}y \right. \\ & \left. + \int_0^h \left[\int_h^y \left(\rho_l \frac{\partial v}{\partial t} - \mu \frac{\partial^2 v}{\partial x^2} \right) \mathrm{d}y \right] y \mathrm{d}y \right]_{x=x_{\mathcal{I}}^{\mathrm{c}}}^{x=x_{\mathcal{I}+1}^{\mathrm{c}}} \ . \end{aligned} \tag{33}$$

This equation is simplified by substituting Eq. (26) as follows:

$$\begin{aligned} \Gamma_I = & \frac{3}{40} \frac{\rho_l h^4}{a_l} \left(\frac{\mathrm{d}^2 Z_{I-1}}{\mathrm{d}t^2} - 2 \frac{\mathrm{d}^2 Z_I}{\mathrm{d}t^2} + \frac{\mathrm{d}^2 Z_{I+1}}{\mathrm{d}t^2} \right) \\ & + \left(-\frac{\epsilon^2}{6} + \frac{3}{5} \right) \frac{\mu h^4}{a_l^3} \left(\frac{\mathrm{d}Z_{I-1}}{\mathrm{d}t} - 2 \frac{\mathrm{d}Z_I}{\mathrm{d}t} + \frac{\mathrm{d}Z_{I+1}}{\mathrm{d}t} \right) \ . \end{aligned} \tag{34}$$

Note that $\epsilon^2/6$ in the RHS of Eq. (34) will be neglected in the following because it is sufficiently small compared to 3/5 according to the assumption $a_l^2 \ll h^2$ (i.e. $\epsilon^2 \ll 1$).

We eventually want Eq. (32) to be expressed with Z_I, and therefore, $\langle u \rangle_{\mathcal{I}}^{\mathrm{L}}$ and $\langle u \rangle_{\mathcal{I}}^{\mathrm{R}}$ are evaluated by the linear interpolations as follows:

$$\langle u \rangle_{\mathcal{I}}^{\mathrm{L}} = \frac{3}{4} \frac{\partial \zeta_{I-1}}{\partial t} + \frac{1}{4} \frac{\partial \zeta_I}{\partial t} \ , \tag{35a}$$

$$\langle u \rangle_{\mathcal{I}}^{\mathrm{R}} = \frac{1}{4} \frac{\partial \zeta_{I-1}}{\partial t} + \frac{3}{4} \frac{\partial \zeta_I}{\partial t} \ . \tag{35b}$$

Substituting Eqs. (34) and (35) into Eq. (32) yields the moment of fluid forces described with Z_I:

$$\begin{aligned}\int_0^h \Sigma_I \; y\mathrm{d}y = &-\frac{\rho_l a_l h^2}{24}\left(\frac{\mathrm{d}^2 Z_{I-1}}{\mathrm{d}t^2}+6\frac{\mathrm{d}^2 Z_{I-1}}{\mathrm{d}t^2}+\frac{\mathrm{d}^2 Z_{I-1}}{\mathrm{d}t^2}\right)\\ &-\frac{\mu a_l}{8}\left(\frac{\mathrm{d}Z_{I-1}}{\mathrm{d}t}+6\frac{\mathrm{d}Z_I}{\mathrm{d}t}+\frac{\mathrm{d}Z_{I+1}}{\mathrm{d}t}\right)\\ &+\frac{3}{40}\frac{\rho_l h^4}{a_l}\left(\frac{\mathrm{d}^2 Z_{I-1}}{\mathrm{d}t^2}-2\frac{\mathrm{d}^2 Z_{I-1}}{\mathrm{d}t^2}+\frac{\mathrm{d}^2 Z_{I-1}}{\mathrm{d}t^2}\right)\\ &+\frac{3}{5}\frac{\mu h^4}{a_l^3}\left(\frac{\mathrm{d}Z_{I-1}}{\mathrm{d}t}-2\frac{\mathrm{d}Z_I}{\mathrm{d}t}+\frac{\mathrm{d}Z_{I+1}}{\mathrm{d}t}\right)\\ &+\frac{h^2}{2}\left(p|_{x=x^{\mathrm{c}}_{\mathcal{I}},y=h}-p|_{x=x^{\mathrm{c}}_{\mathcal{I}+1},y=h}\right)+\tau_I a h \;,\end{aligned} \tag{36}$$

where τ_I is the shear stress by the fluid flow over the canopy defined as follows:

$$\tau_I \overset{\mathrm{def}}{=} \frac{1}{2}\left\langle\tau_l\right\rangle^{\mathrm{R}}_{\mathcal{I}} \; a_l + \tau_{sI} \; a_s + \frac{1}{2}\left\langle\tau_l\right\rangle^{\mathrm{L}}_{\mathcal{I}+1} \; a_l \;, \tag{37}$$

which is the average shear stress in the region between $x^{\mathrm{c}}_{\mathcal{I}}$ and $x^{\mathrm{c}}_{\mathcal{I}+1}$.

Finally, the tip displacements for the the non-uniform deformation obey the following equation:

$$\begin{aligned}&\frac{\rho_s \varphi_s h^2}{3}\frac{\mathrm{d}^2 Z_I}{\mathrm{d}t^2}+\frac{R\rho_l\varphi_l h^2}{24}\left(\frac{\mathrm{d}^2 Z_{I-1}}{\mathrm{d}t^2}+6\frac{\mathrm{d}^2 Z_I}{\mathrm{d}t^2}+\frac{\mathrm{d}^2 Z_{I+1}}{\mathrm{d}t^2}\right)\\ &\quad-\frac{3R}{40}\frac{\rho_l h^4}{a^2\varphi_l}\left(\frac{\mathrm{d}^2 Z_{I-1}}{\mathrm{d}t^2}-2\frac{\mathrm{d}^2 Z_I}{\mathrm{d}t^2}+\frac{\mathrm{d}^2 Z_{I+1}}{\mathrm{d}t^2}\right)\\ &=-\frac{RC}{8}\left(\frac{\mathrm{d}Z_{I-1}}{\mathrm{d}t}+6\frac{\mathrm{d}Z_I}{\mathrm{d}t}+\frac{\mathrm{d}Z_{I+1}}{\mathrm{d}t}\right)\\ &\quad+\frac{3R}{5}\frac{\mu h^4}{a^4\varphi_l^3}\left(\frac{\mathrm{d}Z_{I-1}}{\mathrm{d}t}-2\frac{\mathrm{d}Z_I}{\mathrm{d}t}+\frac{\mathrm{d}Z_{I+1}}{\mathrm{d}t}\right)-\frac{\lambda_1^4}{3}\frac{EI}{A_s h^2}\frac{a_s}{a}Z_I\\ &\quad+\frac{R}{2}\frac{h^2}{a}\left(p|_{(x,y)=(x^{\mathrm{c}}_{\mathcal{I}},h)}-p|_{(x,y)=(x^{\mathrm{c}}_{\mathcal{I}+1},h)}\right)+R\tau_I h \;.\end{aligned} \tag{38}$$

The third term on the left-hand side (LHS) is originated from $\partial v/\partial t$ in Eq. (9b), and the physical meaning is as follows; when the I-th fiber is moved in the $+x$ direction by the hydrodynamic force, the force acts to decrease and increase the y component of the fluid inertia in the $\mathcal{I}$- and $(\mathcal{I}+1)$-th regions, respectively.

Eq. (38) is a finite difference equation for Z_I, and it may be interpreted as an equivalent system

of the following form:

$$\begin{aligned}
&\frac{\rho_s\varphi_s h^2}{3}\frac{\mathrm{d}\dot{Z}}{\mathrm{d}t} + \frac{R\rho_l\varphi_l h^2}{3}\overline{\frac{\mathrm{d}\dot{Z}}{\mathrm{d}t}} - \frac{3R}{40}\frac{\rho_l h^4}{\varphi_l}\frac{\delta^2}{\delta {x_\mathrm{f}}^2}\left[\frac{\mathrm{d}\dot{Z}}{\mathrm{d}t}\right] \\
=& -RC\overline{\dot{Z}} + \frac{3R}{5}\frac{\mu h^4}{a^2\varphi_l^3}\frac{\delta^2\dot{Z}}{\delta {x_\mathrm{f}}^2} - \frac{\lambda_1^4}{3}\frac{EI}{A_s h^2}\frac{a_s}{a}Z \\
&- \frac{Rh^2}{2}\left.\frac{\delta p}{\delta x_\mathrm{f}}\right|_{y=h} + R\tau h \ ,
\end{aligned} \tag{39}$$

where $\overline{\dot{Z}} = (\langle u\rangle^{\mathrm{R}}_{\mathcal{I}} + \langle u\rangle^{\mathrm{L}}_{\mathcal{I}+1})|_{y=h}/2$, and $\delta/\delta x_\mathrm{f}$ and $\delta^2/\delta x_\mathrm{f}^2$ are 2nd-order finite difference operators at the fiber position.

For the purposes of the following section, the physical meanings of the terms in the RHS of Eq. (38) or (39) are summarized. The first term is the damping force, the second term is the diffusion term, the third term is the torsion spring term, and the fourth and fifth terms represent the pressure gradient and the shear force induced by the flow over the canopy. The above terms indicate that the coarse-graining process in Sec. 5 has been enriched in the case of non-uniform deformation. In particular, the motions of the neighboring fibers are reflected in the second term in the LHS and the first term in the RHS of Eq. (38) (correspondingly the LHS and the first term in the RHS of Eq. (21)), and the third term in the LHS and the second term in the RHS of Eq. (38) are the new terms representing the effect of non-uniformity in the motion of the fibers.

For simplicity, the boundary condition for u at the envelope of the canopy is obtained by a linear interpolation in the following:

$$u|_{y=h} \sim \frac{x - x^{\mathrm{c}}_{\mathcal{I}}}{a_l}\left(\frac{\mathrm{d}Z_I}{\mathrm{d}t} - \frac{\mathrm{d}Z_{I-1}}{\mathrm{d}t}\right) + \frac{1}{2}\left(\frac{\mathrm{d}Z_I}{\mathrm{d}t} + \frac{\mathrm{d}Z_{I-1}}{\mathrm{d}t}\right) \qquad (|x - x^{\mathrm{c}}_{\mathcal{I}}| \le a_l/2) \ , \tag{40}$$

which is easily confirmed to be consistent with Eq. (35) and can be reduced to Eq. (19) for the uniform motion case.

6.3 Pressure gradient in the y direction at envelope

From Eq. (9b) and using Eq. (26), the pressure gradient at the envelope is modeled as follows:

$$\left.\frac{\partial p}{\partial y}\right|_{y=h} \sim -\mu\frac{\partial^2 v}{\partial x^2} = -\frac{6\mu h}{a_l^3}\left(\frac{\mathrm{d}Z_I}{\mathrm{d}t} - \frac{\mathrm{d}Z_{I-1}}{\mathrm{d}t}\right) \qquad (|x - x^{\mathrm{c}}_{\mathcal{I}}| \le a_l/2) \ . \tag{41}$$

Note that the term of the first-order derivative of t in Eq. (9b) is neglected for simplicity.

Table 1: Summary of simulation cases and numerical methods. "FSI" means fluid-structure interaction including fibers as individual objects.

	FSI simulation with individual fibers	Simulation with envelope model
Uniform fiber motion (§ 5) Fluid is induced by: Constant pressure gradient.	**Case 1A** (Fig. 5(a)) Fluid: Appendix A.1 Fiber: Appendix A.2	**Case 1B** (Fig. 5(b)) Fluid: Appendix A.1 Envelope: Eq. (21) Discretization: § 7.1
Non-uniform fiber motion (§ 6) Fluid is induced by: Externally-driven cylinder.	**Case 2A** (Fig. 6(a)) Fluid: Same as above. Fiber: Same as above.	**Case 2B** (Fig. 6(b)) Fluid: Same as above. Envelope: Eq. (38) Discretization: § 7.2

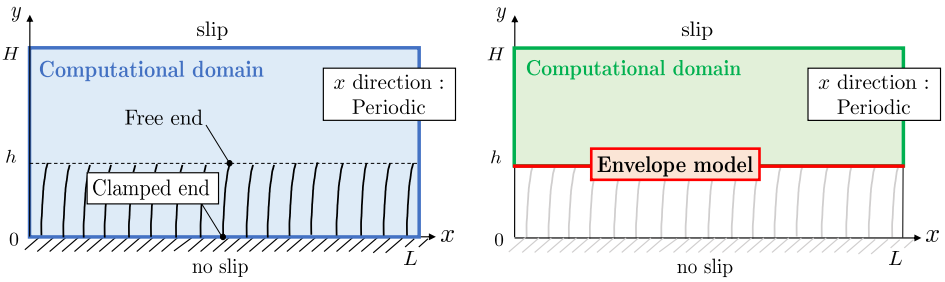

(a) Case 1A (b) Case 1B

Figure 5: Schematic of the boundary conditions (a) for the full simulation of fluid-structure interaction (FSI) with individual fibers, (b) for the simulation with our model under the uniform deformation conditions.

7 Validation cases and numericals

The envelope models in Secs. 5 and 6 are imposed as boundary conditions on the envelope of the canopy in numerical simulations of fluid flow. The results are compared with those obtained by fluid-structure interaction (FSI) simulations including fibers as individual objects. The four cases considered in the following sections are summarized in Tab. 1.

Fig. 5 illustrates the computational domains and the boundary conditions for the two cases of uniform motion of fibers (Cases 1A and 1B) by the FSI simulation (Fig. 5(a)) and the simulation with our envelope model (Fig. 5(b)). In the case of Fig. 5(b), only the fluid motion above the canopy is solved. Considering the mono-sized fibers of length h (see Fig. 5(a)), the fluid domain size for Case 1B is $H - h$ in height and L in width, as illustrated in Fig. 5(b). For both Cases 1A and 1B,

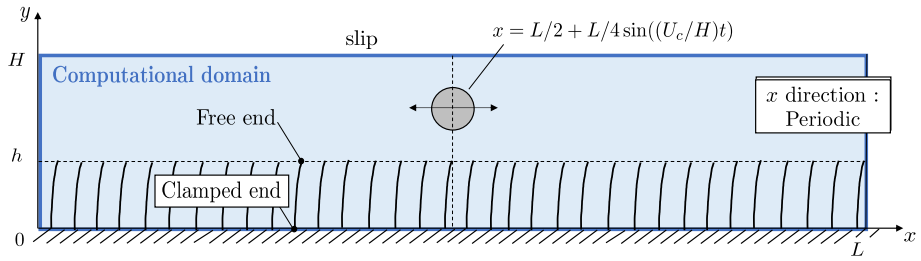

(a) Case 2A

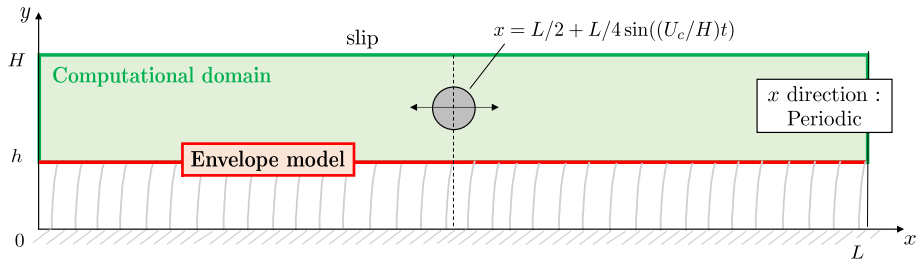

(b) Case 2B

Figure 6: Schematic of the boundary conditions for the case of non-uniform deformation by (a) FSI simulation (Case 1B) and (b) simulation with our envelope model (Case 2B).

a constant pressure gradient is induced in the x direction, and the transient motions of the canopy surface (Z and $\dot{Z}$) and the fluid are compared.

Fig. 6 shows the domains and boundary conditions for the cases of non-uniform motion of fibers (Cases 2A and 2B) by (a) FSI simulation and (b) the envelope model. Non-uniformity is induced by an externally oscillating cylinder above the canopy, which will be described in detail in Sec. 7.4. The restricted domain height for Fig. 6(b) is the same as Fig 5(b).

The governing equations and numerical methods for the FSI simulations are briefly explained in Appendix A.

7.1 Discretization of the uniform envelope model

The envelope model for uniform motion case in the x direction (Eq. (21)) is solved by the Newmark-β method. In the method, $\dot{Z}$ and Z are time updated using $\ddot{Z}$ as follows:

$$\dot{Z}^{n+1} = \dot{Z}^n + \Delta t\gamma\left(\ddot{Z}^n + \ddot{Z}^{n+1}\right), \tag{42a}$$

$$Z^{n+1} = Z^n + \Delta t\dot{Z}^n + \Delta t^2\beta\left(\ddot{Z}^n + \ddot{Z}^n\right), \tag{42b}$$

where the superscripts indicate the time level, and the parameters γ and β are determined as 1/2 and 1/4, respectively, as stable values.

By substituting Eq. (42) into Eq.(21), the following discretized equation is obtained:

$$\begin{aligned}&\left(\frac{4}{\Delta t^2}M_0+\frac{2}{\Delta t}C_0+K_0\right)Z^{n+1}\\&=\left(\frac{4}{\Delta t^2}M_0+\frac{2}{\Delta t}C_0\right)Z^n+\left(\frac{4}{\Delta t}M_0+C_0\right)\dot{Z}^n\\&+M_0\ddot{Z}^n+f_p^n+\frac{3f_d^n-f_d^{n-1}}{2}\ ,\end{aligned}\tag{43}$$

where

$$M_0=\frac{1}{3}\widetilde{\rho}h^2,\quad C_0=RC,\quad K_0=\frac{\lambda_1^4}{3}\frac{EI}{A_sh^2}\frac{a_s}{a},\tag{44a}$$

$$f_p^n=\frac{R}{2}\left(-\frac{\Delta p}{\Delta x}\right)h^2,\tag{44b}$$

$$f_d^n=R\tau h=\frac{R\mu h}{\delta y}\left(u^n|_{y=h+\delta y}-\dot{Z}^n\right)\ .\tag{44c}$$

In Eq. (44c), τ is evaluated with u at a slightly higher level than the envelope, $u^n|_{y=h+\delta y}$. As we use the staggered arrangement of the fluid variables on the Cartesian coordinate system, δy is set to half the cell size.

7.2 Discretization of the non-uniform envelope model

The envelope model for non-uniform deformations (Eq. (38)) is rearranged in a vector form for a total number of N_f fibers as follows:

$$\boldsymbol{M}\ddot{\boldsymbol{Z}}^{n+1}+\boldsymbol{C}\dot{\boldsymbol{Z}}^{n+1}+\boldsymbol{K}\boldsymbol{Z}^{n+1}=\boldsymbol{f}_p^n+\frac{3\boldsymbol{f}_d^n-\boldsymbol{f}_d^{n-1}}{2}\ ,\tag{45}$$

where the matrices and the vectors are given as follows:

$$\boldsymbol{Z} = \begin{pmatrix} Z_1 & Z_2 & \dots & Z_{N_\mathrm{f}} \end{pmatrix}^\mathrm{T} , \tag{46a}$$

$$\boldsymbol{M} = \begin{pmatrix} M_0 & M_1 & & & M_1 \\ M_1 & M_0 & M_1 & & \\ & \ddots & \ddots & \ddots & \\ & & M_1 & M_0 & M_1 \\ M_1 & & & M_1 & M_0 \end{pmatrix} , \tag{46b}$$

$$M_0 = \frac{1}{3}\rho_s\varphi_s h^2 + \frac{1}{4}R\rho_l\varphi_l h^2 + \frac{3}{20}R\frac{\rho_l h^4}{a^2\varphi_l} , \tag{46c}$$

$$M_1 = \frac{1}{24}R\rho_l\varphi_l h^2 - \frac{3}{40}R\frac{\rho_l h^4}{a^2\varphi_l} , \tag{46d}$$

$$\boldsymbol{C} = \begin{pmatrix} C_0 & C_1 & & & C_1 \\ C_1 & C_0 & C_1 & & \\ & \ddots & \ddots & \ddots & \\ & & C_1 & C_0 & C_1 \\ C_1 & & & C_1 & C_0 \end{pmatrix} , \tag{46e}$$

$$C_0 = \frac{3}{4}RC + \frac{6}{5}R\frac{\mu h^4}{a^4\varphi_l^3} , \ C_1 = \frac{1}{8}RC - \frac{3}{5}R\frac{\mu h^4}{a^4\varphi_l^3} \tag{46f}$$

$$\boldsymbol{K} = \mathrm{diag}\left[K_0, \cdots, K_0\right] , \ K_0 = \frac{\lambda_1^4}{3}\frac{EI}{A_s h^2}\frac{a_s}{a} , \tag{46g}$$

$$\boldsymbol{f}_p^n = R\frac{h^2}{2a}\left(\frac{3}{2}\,\Delta\boldsymbol{p}^\mathrm{c}|_{y=h+\delta y} - \frac{1}{2}\,\Delta\boldsymbol{p}^\mathrm{c}|_{y=h+3\delta y}\right) , \tag{46h}$$

$$\Delta\boldsymbol{p}^\mathrm{c} = \begin{pmatrix} p|_{x=x^\mathrm{c}_{N_\mathrm{f}}} - p|_{x=x^\mathrm{c}_1} \\ p|_{x=x^\mathrm{c}_1} - p|_{x=x^\mathrm{c}_2} \\ \vdots \\ p|_{x=x^\mathrm{c}_{N_\mathrm{f}-1}} - p|_{x=x^\mathrm{c}_{N_\mathrm{f}}} \end{pmatrix} , \tag{46i}$$

$$\boldsymbol{f}_d^n = \frac{R\mu h}{\delta y}\left(\bar{\boldsymbol{u}}^n|_{y=h+\delta y} - \dot{\boldsymbol{Z}}\right) , \tag{46j}$$

$$\bar{\boldsymbol{u}}^n = \begin{pmatrix} \bar{u}_1^n & \bar{u}_2^n & \dots & \bar{u}_{N_\mathrm{f}}^n \end{pmatrix}^T , \ \ \bar{u}_I \overset{\mathrm{def}}{=} \frac{1}{a}\int_{x^\mathrm{c}_\mathcal{I}}^{x^\mathrm{c}_{\mathcal{I}+1}} u \ \mathrm{d}x . \tag{46k}$$

Note that $\boldsymbol{M}$ and $\boldsymbol{C}$ are tridiagonal matrices except for the top-right and bottom-left components, which reflect the periodic boundary condition in the x direction (see Fig. 6), and the first and last components of $\boldsymbol{f}_p^n$ also reflect the periodic structure. Eq. (46h) means a linear extrapolation for the pressure at the envelope. By substituting Eqs. (46) into Eq.(45) and rearranging in a form of the

Newmark-β method, the following discretized equation for $\boldsymbol{Z}^{n+1}$ is obtained:

$$\left(\frac{4}{\Delta t^2}\boldsymbol{M}+\frac{2}{\Delta t}\boldsymbol{C}+\boldsymbol{K}\right)\boldsymbol{Z}^{n+1}$$
$$=\left(\frac{4}{\Delta t^2}\boldsymbol{M}+\frac{2}{\Delta t}\boldsymbol{C}\right)\boldsymbol{Z}^{n}+\left(\frac{4}{\Delta t}\boldsymbol{M}+\boldsymbol{C}\right)\dot{\boldsymbol{Z}}^{n} \tag{47}$$
$$+\boldsymbol{M}\ddot{\boldsymbol{Z}}^{n}+\boldsymbol{f}_p^n+\frac{3\boldsymbol{f}_d^n-\boldsymbol{f}_d^{n-1}}{2}\,, \tag{48}$$

which corresponds to Eq. (43), and $\dot{\boldsymbol{Z}}^{n+1}$ is given by the similar equation to Eq. (42a).

7.3 Numerical methods for the other equations and terms

For the FSI simulation cases (Cases 1A and 2A, correspondingly Figs. 5(a) and 6(a), respectively), the fluid-fiber interaction is solved by an immersed boundary method proposed by Huang and Sung (2009), which is briefly explained in Appendix. A.3.

For Cases 1B and 2B (Figs. 5(b) and 6(b), respectively), the fluid motion above the envelope is solved by a second order finite difference method, and the incompressible velocity and pressure fields are coupled by the simplified MAC (SMAC) method (Amsden and Harlow 1970). Both convective and viscous terms are time updated using the second order Adams-Bashforth method.

In the validation cases (Sec. 8), the thickness of the fiber a_s is typically covered by a few grid points for the FSI simulations. On the other hand, the envelope models are not designed to resolve at the level of individual fibers, and indeed, the model can handle under-resolved conditions, $a<\Delta x$, where Δx is the grid spacing, as will be shown in Sec. 8.1. Therefore, to stress the intention of targeting coarse resolution cases by the envelope model for the non-uniform fiber motion, the boundary conditions of fluid velocities and pressure (Eqs. (40), (27), and (41)) are simplified by replacing a_l by a, as follows:

$$u|_{y=h}\sim\frac{x-x_{\mathcal{I}}^{\mathrm{c}}}{a}\left(\frac{\mathrm{d}Z_I}{\mathrm{d}t}-\frac{\mathrm{d}Z_{I-1}}{\mathrm{d}t}\right)+\frac{1}{2}\left(\frac{\mathrm{d}Z_I}{\mathrm{d}t}+\frac{\mathrm{d}Z_{I-1}}{\mathrm{d}t}\right), \tag{49a}$$
$$v|_{y=h}\sim\frac{3h}{a^3}\left(\frac{\mathrm{d}Z_I}{\mathrm{d}t}-\frac{\mathrm{d}Z_{I-1}}{\mathrm{d}t}\right)\left[(x-x_{\mathcal{I}}^{\mathrm{c}})^2-\frac{a^2}{4}\right], \tag{49b}$$
$$\left.\frac{\partial p}{\partial y}\right|_{y=h}\sim-\frac{6\mu h}{a^3}\left(\frac{\mathrm{d}Z_I}{\mathrm{d}t}-\frac{\mathrm{d}Z_{I-1}}{\mathrm{d}t}\right). \tag{49c}$$

7.4 Simulation parameters

For all cases in Tab. 1, the reference length is H. The height and width of the fibers are fixed at $h/H = 0.4$ and $a_s/H = 0.03$, respectively, to keep the value of Eq. (4) the same throughout the numerical simulations hereafter. The size of the fluid-filled region is varied for the following two values: $a_l/H = 0.032$ and 0.095 (correspondingly, $\epsilon = a_l/h = 0.08, 0.23$ and $a/h = 1/6.4, 1/3.2$, respectively).

For Cases 1A and 1B (uniform motion), the reference velocity is the friction velocity u_τ defined at the bottom wall in the absence of canopy, and the external pressure gradient $(\Delta p/\Delta x)(H/(\rho_l u_\tau^2))$ in Eq. (7) is fixed at -1. The longitudinal (x) domain size and the time step size are set at $L/H = 2$ and $\Delta t/(H/u_\tau) = 2.0 \times 10^{-5}$, respectively. The numbers of the grid points in the x and y directions are $(N_x, N_y) = (160, 80)$ for Case 1A. For Case 1B, the longitudinal resolution L/N_x is the same as above, whereas the displaced domain height $(1 - h/H)$ is covered by the number of grid points $N_y' = 0.6N_y$, unless specified otherwise. Therefore, the grid spacing is uniformly $\Delta x/H = \Delta y/H = 1/80$, and the standard resolution of the inter-fiber distance is $a/\Delta x = 10$. For the uniform motion FSI case (Case 1A), the other parameters are set as follows: $EI(a_s/A_s)/(\rho_l {u_\tau}^2 H^3) = 5.0 \times 10^{-3}$, $\rho_s/\rho_l = 1.1$, $Re_\tau = Hu_\tau/\nu = 10$, and $N_\mathrm{f} = 32$ and 16 for $a/h = 1/6.4$ and $1/3.2$, respectively. For the uniform envelope case (Case 1B), the parameter values are the same as for the FSI simulation, except that the height of the fluid domain is $1 - h/H = 0.6$. The values of the correction factor R and the damping coefficient $C/(\rho_l u_\tau H)$ are determined based on the steady FSI solution, which will be explained later.

For the case of non-uniform motion (Cases 2A and 2B; Fig. 6), a wider computational domain of $L/H = 4$ is used and $\Delta p/\Delta x$ is set to zero. To induce non-uniform motion of the fibers, a cylinder of diameter $0.25H$ is used with the prescribed motion of the center coordinates as $x(t)/H = 2 + \sin((U_c/H)t), y/H = 0.7$, unless specified otherwise. The maximum velocity of the cylinder U_c is selected as the reference velocity. The same grid spacing ($\Delta x/H = \Delta y/H = 1/80$) is used, and the other conditions and parameters are the same as in Cases 1A and 1B, except that the Reynolds number and the time step size are $Re_c = HU_c/\nu = 10$ and $\Delta t/(H/U_c) = 1.0 \times 10^{-5}$, respectively. Note that, the values of R and $C/(\rho_l U_c H)$ for Case 2B are the same as those in Case 1B because the hydrodynamic force model for the case of non-uniform motion is developed in the same way as in the uniform motion case.

8 Results and discussion

8.1 Case of uniform motion of fibers

First, the parameters R and C are identified by fitting the time response of Z obtained from the FSI simulation. The steady displacement is estimated by eliminating the unsteady terms in Eq. (21) as

$$\frac{Z_{\text{steady}}}{H} = \frac{R}{H}\frac{-(\Delta p/\Delta x)ah^2/2 + (\mu ah/\delta y)u|_{y=h+\delta y}}{(EI/A_s h^2)a_s\lambda_1^4/3} \ . \tag{50}$$

Using the steady displacement (Z_{steady}) obtained from the FSI simulation, R is determined, and then C is estimated to match the damping response of Z. Based on this process, $(R, C/(\rho_l u_\tau H)) = (0.28, 0.16)$ and $(0.26, 0.16)$ for $a/h = 1/3.2$ and $1/6.4$ are determined, respectively. Fig. 7 compares the time series of the x components of (a) displacement and (b) velocity at the canopy surface obtained by the envelope model and the FSI simulation for the following two inter-fiber distances: $a/h = 1/6.4$ and $1/3.2$. Eq. (50) is also plotted. The figure shows that the envelope model (solid lines) reproduces well the transient response of the fibers by the FSI simulation (dashed lines), suggesting that the interaction between the fluid and the fibers can be described by a mass-spring-damper system (Eq. (21)) for small and uniform displacement conditions.

Fig. 8(a) compares the fluid velocity fields and the fiber deformations at $a/h = 1/6.4$ obtained by the FSI simulation and the envelope model at the non-dimensional time $t/(H/u_\tau) = 5.0$. Note that, for the envelope model, the deflections of the fibers are illustrated by linear interpolation between the hinged point $(x, y) = (x_I, 0)$ and the tip $(x, y) = (x_I + Z_I, h)$. To check the applicability of the model to a dilute situation, we also investigate a case with a larger inter-fiber spacing of $a/h = 1/3.2$. As observed in the snapshot in Fig. 8(b), the increased deflection of the fibers by the FSI simulation is again reproduced by the envelope model.

However, as shown in Fig. 8, the envelope model slightly underestimates the magnitude of the fluid velocities (green) compared to those of the FSI simulation (blue). Fig. 9 compares the transient states of the y distributions of the longitudinal velocity component for $a/h = 1/6.4$ (top row) and $1/3.2$ (bottom row) in a mid-domain cross-section of $x/H = 1 + 1/16$ where one fiber is located. The horizontal dashed line indicates the canopy surface ($y/H = 0.4$). The evolution of the velocity profile for $a/h = 1/6.4$ is reproduced by our envelope model (Figs. 9(a) $\sim$ 9(c)), whereas relatively larger

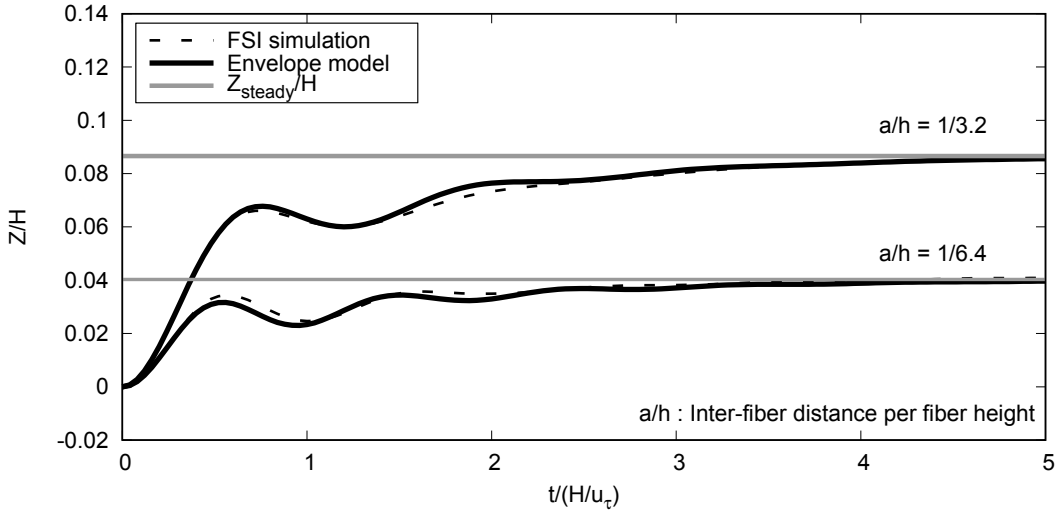

(a) Displacement

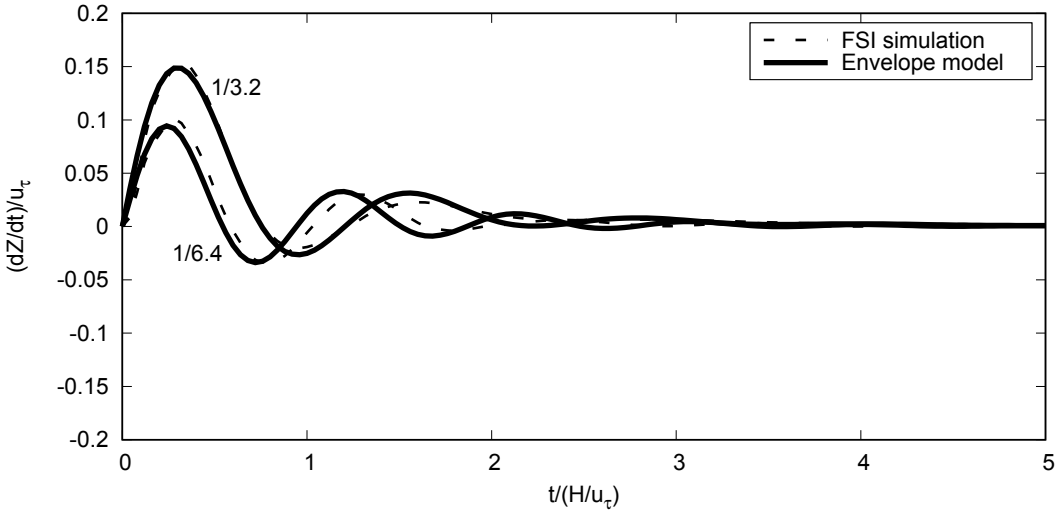

(b) Tip velocity

Figure 7: Time series of the x component of (a) displacement and (b) tip velocity at the canopy surface for two the inter-fiber distances: $a/h = 1/6.4, 1/3.2$. The solid lines show the results by our envelope model and the dashed lines are by the FSI simulation.

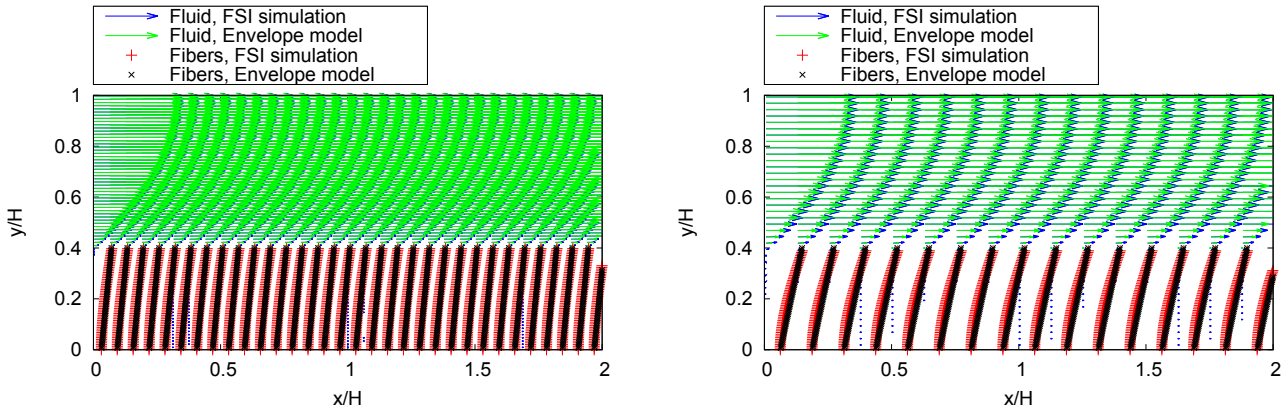

(a) $a/h = 1/6.4$ (b) $a/h = 1/3.2$

Figure 8: Flow fields of the uniform motion cases for the inter-fiber distances a/h =(a)1/6.4 and (b)1/3.2, at the non-dimensional time $t/(H/u_\tau) = 5.0$ after reaching steady state. The arrows are plotted at every 10 and 2 grid points in the x and y directions, respectively. The deflection of the fibers obtained by the proposed model (black) are in good agreement with those obtained by the FSI simulation (red). The dotted lines represent the x displacements of the canopy surface.

Table 2: Cases to investigate the effect of grid resolution. The numbers of grid points in the y direction, N_y and N'_y, cover the computational height 1 and $1 - h/H$, respectively.

Case	Simulation type	$N_x \times N_y(N'_y)$	$\Delta x/H$	$a/\Delta x$
1A	FSI	320×160	0.00625	10
1B-1	Envelope	320×96	0.00625	10
1B-2	Envelope	80×24	0.025	2.5
1B-3	Envelope	30×9	0.067	0.94

differences in the fluid velocities are observed for the case of larger inter-fiber region ($a/h = 1/3.2$) as shown in Fig. 9(d)∼9(f). This is because the fluid velocity at the envelope does not fully coincide with the tip velocity $(\mathrm{d}Z/\mathrm{d}t)/u_\tau$ in the FSI simulation due to the non-negligible effect of incoming flow into the inter-fiber region.

The advantage of the present envelope model may be that Eq. (21) does not depend on the local coordinate x. Therefore, the results of the envelope model are expected to be insensitive to the grid resolution, which is tested by varying the spatial resolution for the cases summarized in Tab. 2. Cases 1A and 1B-1 are identical to the simulations by the FSI and envelope model simulations in Fig. 8(a), respectively, and Cases 1B-2 and 1B-3 use larger grid spacing, $\Delta x/H$. In particular, Δx in Case 1B-3 is larger than the inter-fiber distance a. Fig. 10 compares the time series of the tip

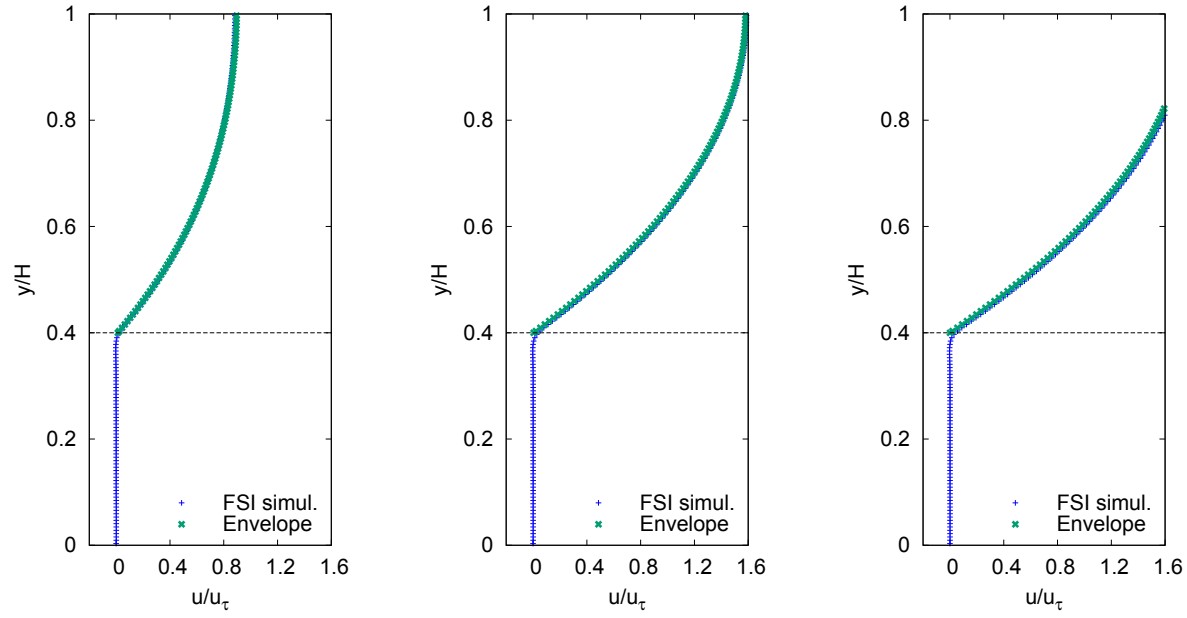

(a) $t/(H/u_\tau) = 1.0$ (b) $t/(H/u_\tau) = 3.0$ (c) $t/(H/u_\tau) = 5.0$

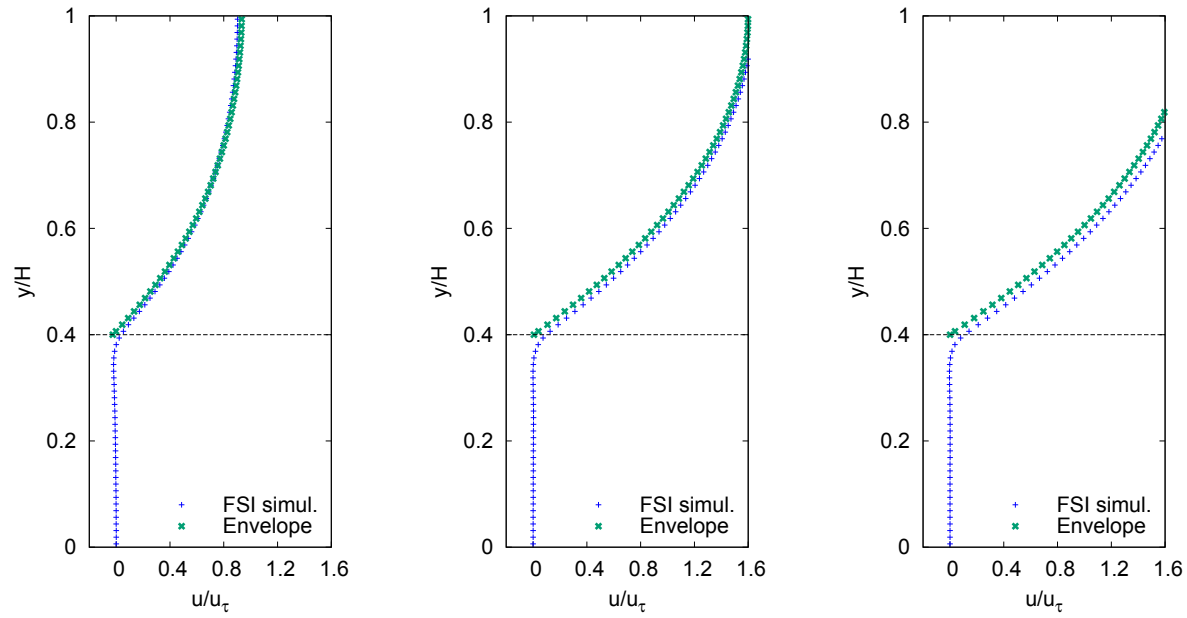

(d) $t/(H/u_\tau) = 1.0$ (e) $t/(H/u_\tau) = 3.0$ (f) $t/(H/u_\tau) = 5.0$

Figure 9: Wall-normal profiles of the x component of the fluid velocity at $t/(H/u_\tau) =$ (a)(d) 1.0, (b)(e) 3.0, and (c)(f) 5.0. The top and bottom rows are $a/h = 1/6.4$ and $1/3.2$, respectively. The result of the FSI simulation is shown in blue and that of the envelope model in green. The black dashed line indicates the canopy surface where the envelope model is applied.

displacements and velocities for the cases in Tab. 2, and the graphs show that our model produces similar results to one another.

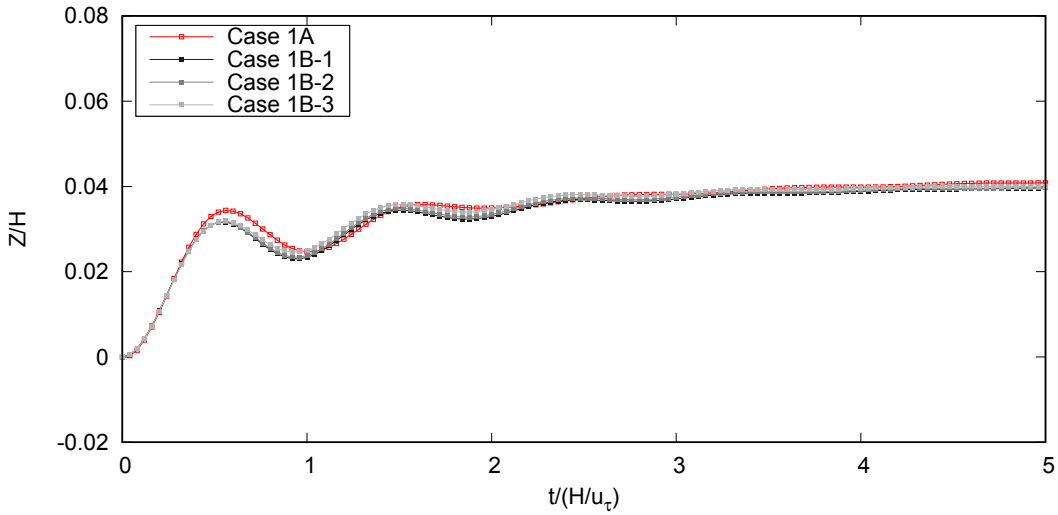

(a) Displacement

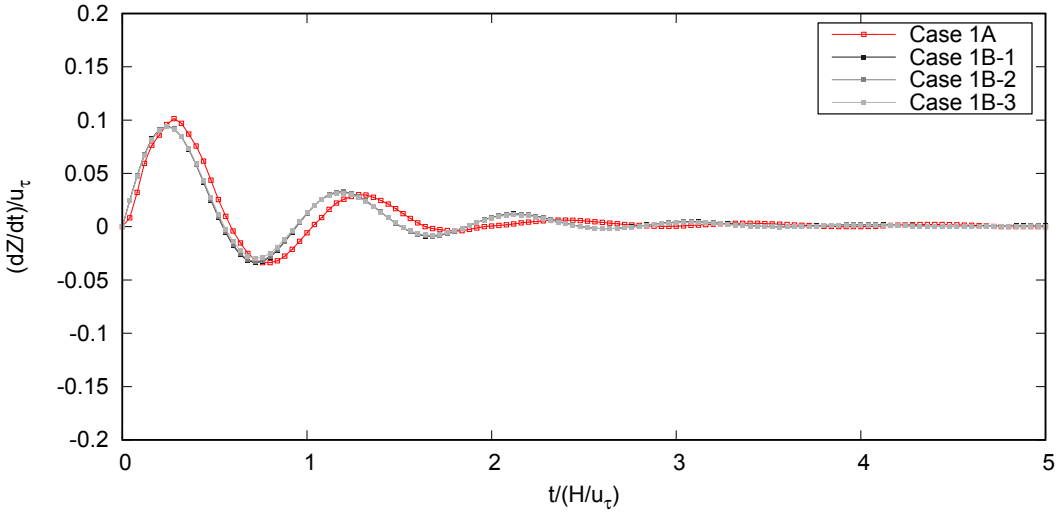

(b) Tip velocity

Figure 10: Comparison of the time series of the x component of (a) the displacement and (b) tip velocity of the envelope for different spatial resolutions.

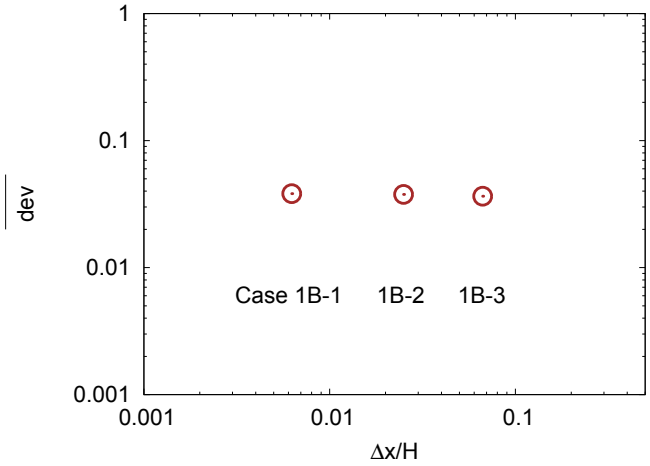

Figure 11: Time-averaged deviation in $(\mathrm{d}Z/\mathrm{d}t)/u_\tau$ for Case 1B-m ($m = 1, 2, 3$) with respect to Case 1A (see Eq. (51)) plotted as a function of grid spacing. Each grid spacing corresponds to a case specified in Tab. 2.

The average deviation of the tip velocity obtained by the envelope model from that obtained by the FSI simulation is evaluated as follows:

$$\overline{\mathrm{dev}} = \frac{1}{N_\mathrm{c}} \sum_{n}^{N_\mathrm{c}} \frac{|\ \mathrm{d}Z/\mathrm{d}t^n_{\text{Case 1B-}m} - \mathrm{d}Z/\mathrm{d}t^n_{\text{Case 1A}}\ |}{\max|\mathrm{d}Z/\mathrm{d}t^n_{\text{Case 1A}}|}\ , \tag{51}$$

where the superscript n indicates the time level and $m = 1, 2, 3$. The average is calculated with a total of N_c ($= 181$) data sets at a constant time interval until the flow field reaches steady state. Fig. 11 plots $\overline{\mathrm{dev}}$ as a function of grid spacing $\Delta x/H$, and it shows that the deviations in $(\mathrm{d}Z/\mathrm{d}t)/u_\tau$ are insensitive to the grid spacing even at the coarsest grid spacing (Case 1B-3).

The above results suggest that the simulation cost by the present envelope model is also independent of the number of fibers N_f (and, in turn, independent of the inter-fiber spacing a/h).

8.2 Case of non-uniform motion of fibers

Fig. 12 shows the snapshots of the instantaneous velocity field and fibers by the FSI and envelope-model simulations at $t/(H/U_c)$ = (a)1.0, (b)3.0, and (c)5.0. At the instant of Fig. 12(a), the cylinder moves to the left and then the fluid is induced to flow in the same direction with a small time lag. Even in a region far away from the cylinder, the fibers are pushed to the left, while the fibers directly below the cylinder are deflected to the right. Fig. 12(b) is the instant just before the cylinder stops,

and in Fig. 12(c) the cylinder travels to the right. For the fluid velocities and fiber deflections at all the instances ($t/(H/U_c) = 1.0, 3.0$ and 5.0), the results by our model show reasonable agreement with those by the FSI simulation. In particular, the directions and the magnitudes of the fluid velocity by our model above $y/H = 0.4$ are almost the same as the FSI simulation result.

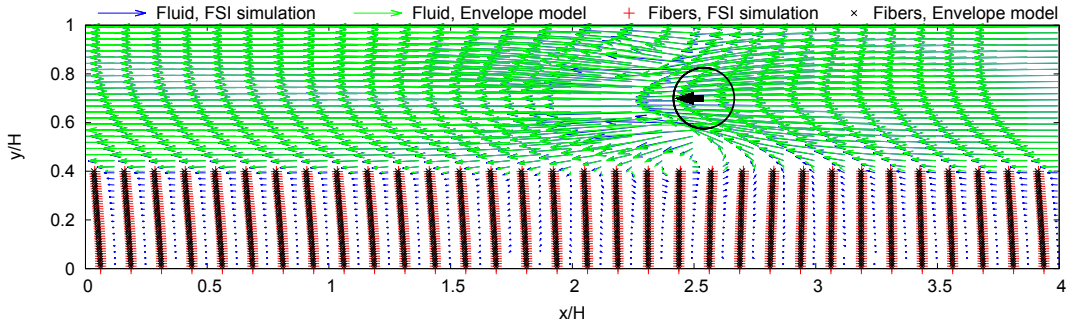

(a) $t/(H/U_c) = 1.0$

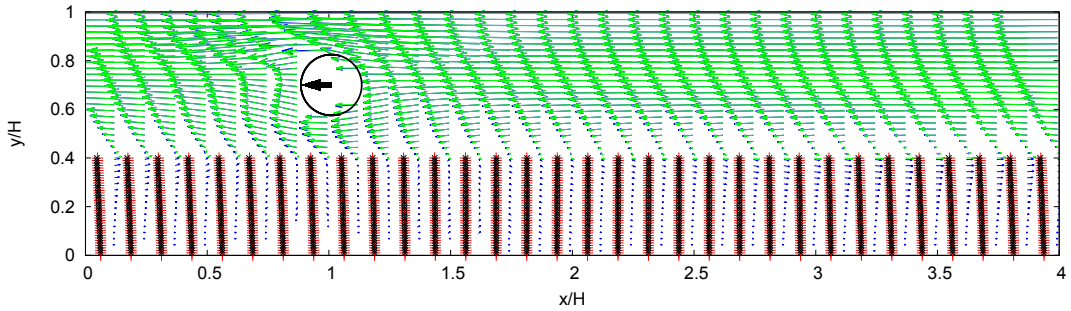

(b) $t/(H/U_c) = 3.0$

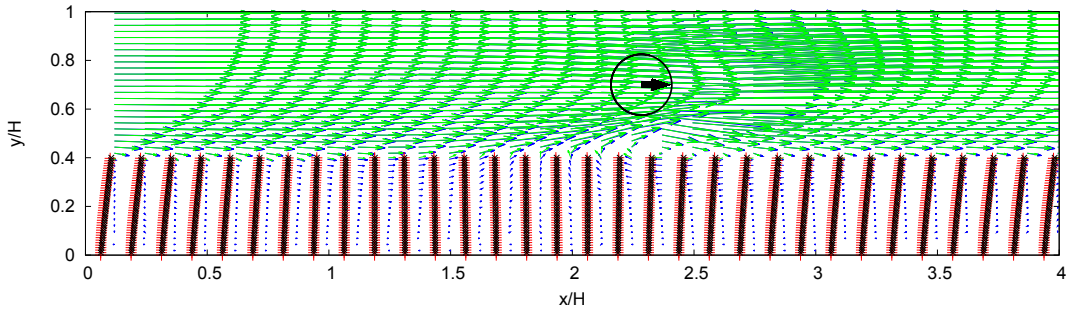

(c) $t/(H/U_c) = 5.0$

Figure 12: Flow field of the non-uniform condition at $t/(H/U_c) =$ (a) 1.0, (b) 3.0, and (c) 5.0. The cylinder (shown as the black circle) moves one period from $x/H = 3.0$. The velocity vectors are shown by the arrows (blue, the FSI simulation; green, the envelope model) and those are plotted at every 10 and 2 grid points in the x and y directions, respectively. The arrows in the region occupied by the cylinder are the velocity of the fluid in the wake. The fiber deformations are shown by red symbols (the FSI simulation) and black symbols (the envelope model).

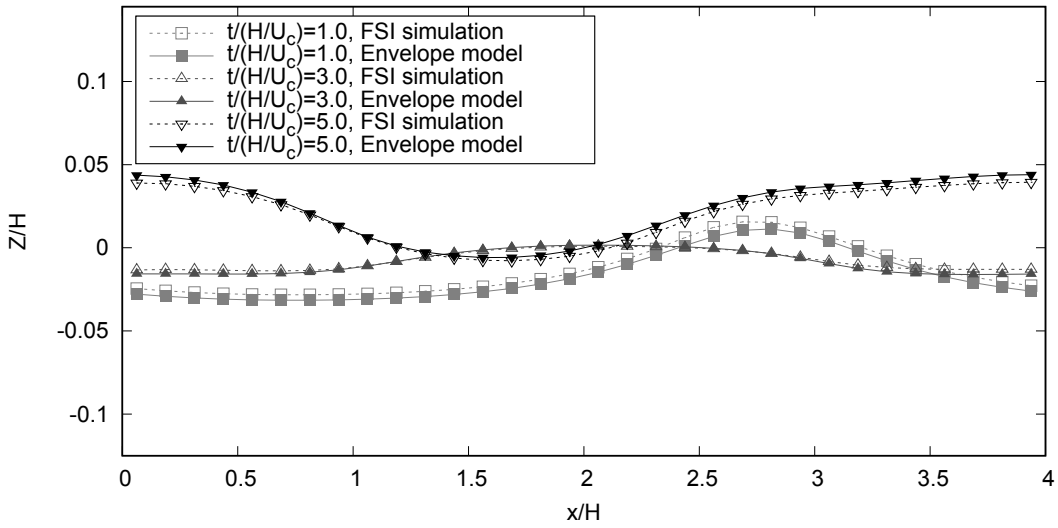

(a) Displacement

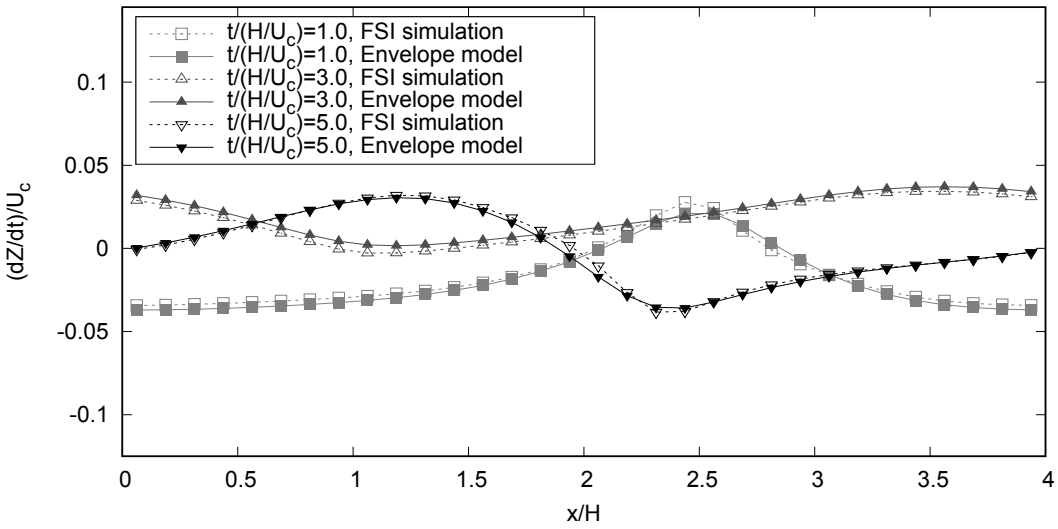

(b) Tip velocity

Figure 13: Longitudinal distributions of the x component of the (a)displacement and (b)velocity of the envelope at $t/(H/U_c) = 1.0, 3.0, 5.0$.

Fig. 13 shows the profiles of the x component of (a) displacement and (b) velocity at the tip of the fibers at the same instants as in Fig. 12. From the figure, both displacement and tip velocity predicted by the envelope model agree well with the FSI simulation result.

To investigate the dominant factors in the envelope model, Fig. 14 compares the time evolution of the following terms; the LHS terms in Eq. (38) (represented as LHS in the figure) and the respective terms in the right-hand side (represented as 1st $\sim$ 5th in RHS). The values of the terms are monitored

at a point above the fiber near the domain center ($x/H = 2 - 1/16$). The figure suggests that the 2nd $\sim$ 5th terms (respectively, diffusion (red), torsion spring (grey), pressure difference (black), and shear force (green) terms, respectively) are active. In particular, the locally-strong events of diffusion at $t/(H/U_c) = 1.7$ and 4.7 in Fig. 14 suggest the direct influence of the passage of the cylinder above the probe position.

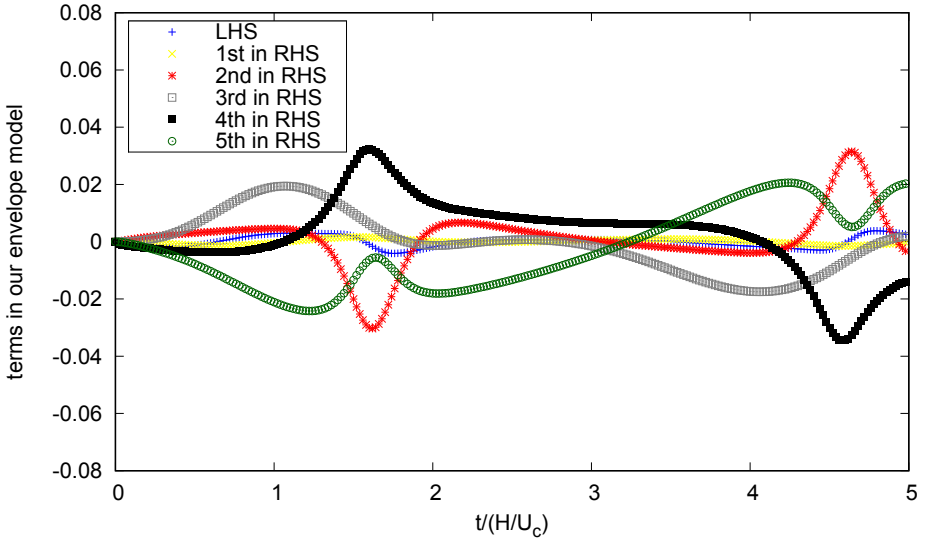

Figure 14: Time series of the values of the terms in the envelope model (Eq. (38) for non-uniform deformation of fibers). We focus on the fibers around $x/H = 2-1/16$, where 1/16 is half the distance between two neighboring fibers. In the figure, "LHS" means the left-hand side in Eq. (38), and the respective terms in Eq. (38) are represented as "1st$\sim$5th in RHS".

Fig. 15 compares the time series of the x component of the fluid velocity u/U_c at the following y/H levels: (a) at the canopy surface $y/H = h/H$, (b) just below the envelope $y/H = (h - \Delta y)/H$, and (c) deep inside the canopy $y/H = 0.35$, where the fluid velocities are obtained by interpolation with the velocities of the neighboring fibers $\partial\zeta/\partial t$. The solid and broken lines are by the envelope model and the FSI simulation, respectively, and the colors indicate the probe position: $x/H = 1.0$ and 3.0 in black in grey, respectively. At all the y/H levels, the time-varying trends of u/U_c are reproduced by the envelope model, although there are some time ranges where the deviations are slightly large, especially in Fig. 15(a). We suspect that the main factor for the deviation is the large velocity difference across the envelope (i.e. inside and outside the canopy); the fluid velocity at $y/H = h/H$ is strongly influenced by the flow over the canopy, especially when the induced velocity by

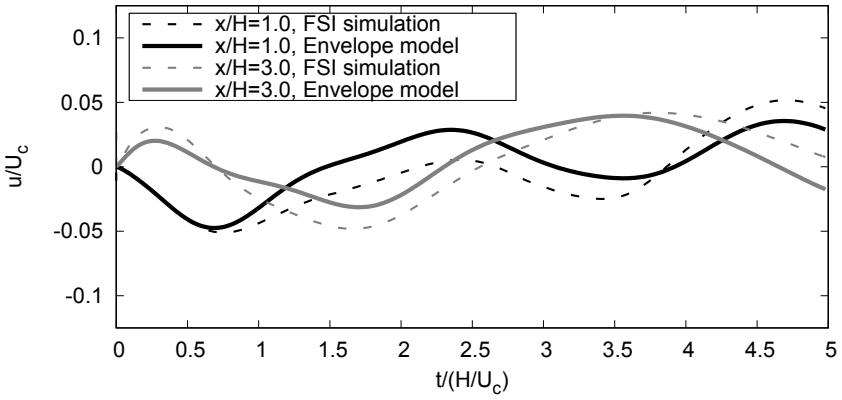

(a) $y = h$

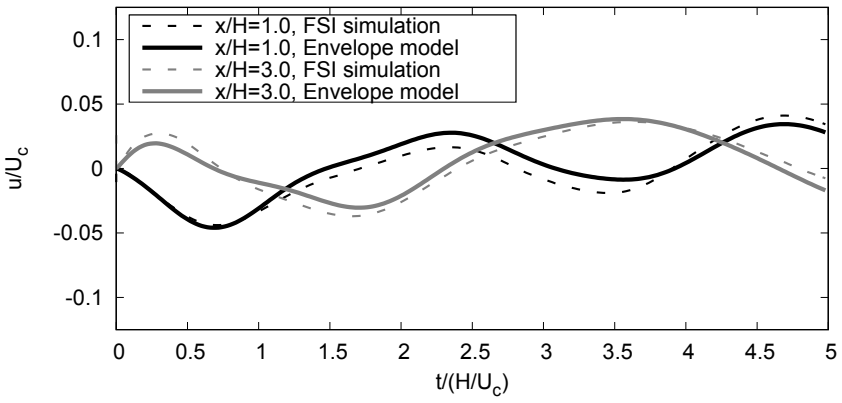

(b) $y = h - \Delta y$

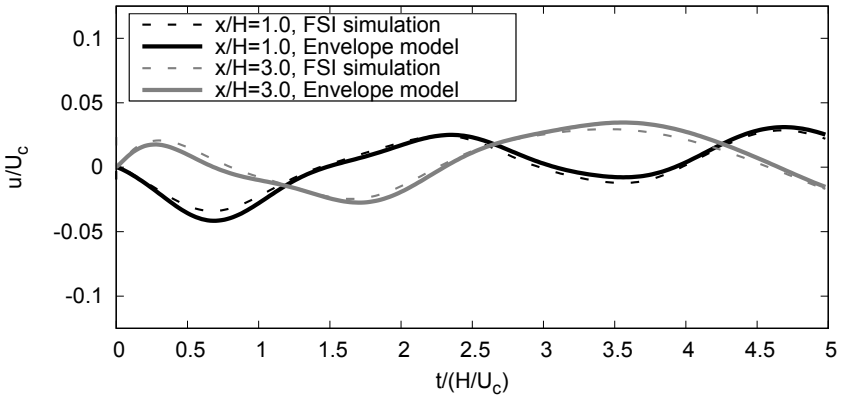

(c) $y = 0.35H$

Figure 15: Time series of the x components of the fluid velocity at $x/H = 1.0$ (black) and 3.0 (grey) for three different wall-normal levels: (a) at the envelope, (b) just below the envelope and (c) inside the canopy. The solid lines are the results by our envelope model, and the dashed lines are by the FSI simulation. Both $x/H = 1.0$ and 3.0 are the center of the inter-fiber regions ($x/H = x_{\mathcal{I}}^{\mathrm{c}}/H$). The solid lines are shown by interpolation of the velocities of the neighboring fibers.

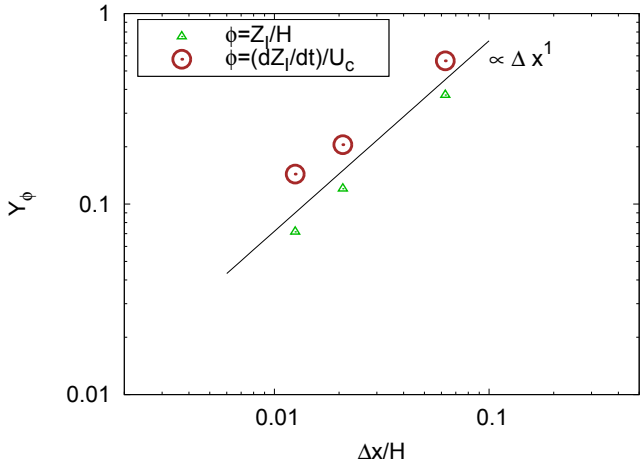

Figure 16: Grid dependency of Y_ϕ for $\phi = Z/H$ (triangular symbol) and $(\mathrm{d}Z/\mathrm{d}t)/U_c$ (circular symbol). The normalized inter-fiber distance is fixed at $a/h = 1/3.2$ and the parameter values are $(R, C/(\rho_l U_c H)) = (0.28, 0.16)$.

the passing cylinder dominates at about $t/(H/U_c) = 2.0$. The same reason also applies to Fig. 15(b). On the other hand, from Fig. 15(c), the results by the envelope model show good agreement with those of the FSI simulation. This is because the flow inside the canopy is less influenced by the flow above the canopy, and therefore, the linear interpolations in Eq. (35) are reasonable treatments. The longitudinal distributions of the fluid velocity u also support the treatment of interpolation, as summarized in Appendix B.

The effect of grid resolution on the model prediction is investigated by varying $\Delta x/H$. However, under a low resolution, the flow around a cylinder may not be sufficiently resolved. To avoid this problem, a cylinder with twice the diameter of Case 2 is used only in this problem and oscillated along the line of $y/H = 0.9$. The spatial resolution is varied as $\Delta x/H = 0.0125, 0.0208, 0.0625$, which correspond to $a/\Delta x = 10, 6, 2$, respectively. Time averaged deviations of displacement and tip velocity are defined as follows:

$$Y_\phi \stackrel{\text{def}}{=} \frac{\dfrac{1}{T}\displaystyle\int_0^T \mathrm{d}t \sqrt{\sum_{I=1}^{N_\mathrm{f}} \left(\phi_\mathrm{FSI}(t) - \phi_\mathrm{Env}(t)\right)^2}}{\max\limits_t \left[\sqrt{\sum_{I=1}^{N_\mathrm{f}} \phi_\mathrm{FSI}^2(t)}\right]}, \tag{52}$$

where ϕ is either $Z(t)/H$ or $(\mathrm{d}Z/\mathrm{d}t)/U_c$, and the subscript "Env" means the envelope model. The averaging period T is set as $T = 1.0H/U_c$, which is sufficiently long compared with the harmonic

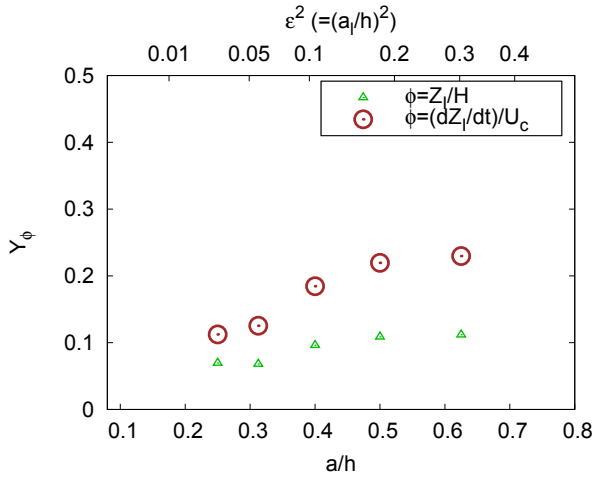

Figure 17: Trend of the time-averaged deviations Y_ϕ of the tip displacement ($\phi = Z$) and velocity ($\phi = \mathrm{d}Z/\mathrm{d}t$) plotted against the normalized inter-fiber distance a/h. Smaller a/h corresponds to higher number density of fibers. The parameter values are $(R, C/(\rho_l U_c H)) = (0.27, 0.16)$, $(0.28, 0.16)$, $(0.29, 0.19)$, $(0.31, 0.21)$, $(0.32, 0.22)$ for $a/h = 1/4.0, 1/3.2, 1/2.5, 1/2.0, 1/1.6$, respectively.

period of fibers $2\pi/\omega_{\mathrm{free}} \sim 0.7H/U_c$. Fig. 16 shows the grid dependency of Y_ϕ. The results of the envelope model exhibit convergence at the first-order rate with respect to $\Delta x/H$ for the unsteady problem.

The effect of number density of fibers is studied to investigate the applicable range of the model. The number of fibers are varied in the following range: $N_{\mathrm{f}} = 16, 20, 25, 32, 40$, which correspond to $a/h = 1/1.6, 1/2.0, 1/2.5, 1/3.2, 1/4.0$, respectively. Note that the largest inter-fiber distance ($a = h/1.6$) is the same as the cylinder diameter ($0.25H$). The other parameter values are the same as those in Cases 2A and 2B. Fig. 17 shows the trend of Y_ϕ against the normalized inter-fiber distance a/h (lower axis) and the square of the aspect ratio of the fluid-filled region ϵ^2 ($= a_l^2/h^2$) (upper axis). The values of Y_ϕ increase with a/h for both the displacement and velocity. This is because, as the inter-fiber distance increases, the flow induced by the cylinder perturbs the inter-fiber region, resulting in the violation of the diffusion-dominant assumption (Assumptions 3 and 4; $a_l/h = \epsilon \lesssim 1$, $\epsilon^2 \ll 1$ and $\epsilon^2\, Re \ll 1$). Considering that the Reynolds number for the inter-fiber flow is $Re = h\dot{Z}/\nu < 1$ in the present study, the above conditions are simplified to the following geometric conditions: $\epsilon \lesssim 1$ and $\epsilon^2 \ll 1$. From this discussion, these geometric relations may provide a reasonable measure to assess the applicable range of the envelope model, and $\epsilon^2 = O[10^{-2}]$ is a practical range for the present envelope model.

9 Conclusion

Boundary conditions for the fluid flow above a canopy have been proposed at the envelope of the fiber tips in two dimensions by coarse graining the interaction process between fluid and fiber motions in the canopy for small displacements.

By assuming that the aspect ratio (ϵ) of surface-to-surface distance of the fibers to the fiber length is $\epsilon \lesssim 1$ and $\epsilon^2 \ll 1$ and the Reynolds number is $\epsilon^2 Re \ll 1$, the moment of the fluid forces acting on the fibers (replicated as rigid rods hinged to a flat wall) was evaluated in terms of the fiber motion, and finally the time-dependent equation for the tip displacement was obtained. The obtained equation takes a form of a mass-spring-damper equation for the tip displacements of the fibers. The advantage of our models is that the solution of the equation was simply used as the boundary condition at the canopy envelope for the fluid motion above it, which enabled reduction of the computational cost.

The simulations with the envelope boundary conditions reproduced the motions of the fluid and the fiber tips well compared to the result of the fluid-fiber interaction (FSI) simulation with elastic fibers as individual objects. The envelope model for uniform deformation was insensitive to the grid resolution, even at grid spacings larger than the inter-fiber distance, whereas, for the case of non-uniform deformation, the results of our model converged to the FSI simulation results at about a first order rate of the grid spacing, suggesting that our envelope models correctly reflect the fluid motion in the canopy.

As the non-uniformity of canopy motion develops, the effects of fluid inertia along the fiber stems and the diffusion of tip velocities become non-negligible. This tendency can become significant when the inter-fiber distance is smaller (i.e. high number density of fibers). From the discussion of the discrepancy between the FSI results and the model predictions, the applicable range of inter-fiber distances is described by the geometric conditions for fluid motion in the inter-fiber region to be diffusion dominated.

Our models suggest that, under low Reynolds number and dense distribution of fibers, the propagation of fiber motion is dominated by a parabolic-type equation (i.e., diffusion) associated with hydrodynamic and elastic effects, and the present analysis will help us to understand the mechanisms of canopy behavior.

The extension of the model to general three-dimensional situations and the relaxation of the small displacement condition are the subject of on-going study of the present authors.

Appendix

A Fluid-fiber interaction problem with individual fibers

A.1 Fluid motion

The fluid is assumed to have constant density ρ_l and constant kinetic viscosity ν. The governing equations of the fluid motion are the equation of continuity and the Navier-Stokes equations as shown in Eq. (7). The governing equations of the fluid are solved by a finite difference method. The variables are defined on the staggered arrangement on a Cartesian mesh. The incompressible velocity and pressure fields are coupled by a fractional step method. Both convective and viscous terms are time updated with the second order Adams-Bashforth method.

A.2 Fiber motion

The equation of motion for the fibers considering the geometric non-linearity is as follows:

$$\rho_s \frac{\partial \boldsymbol{x}}{\partial t} = \nabla_X \cdot \left(\boldsymbol{S} \cdot \boldsymbol{F}^T \right) + \boldsymbol{F}_f, \tag{A1}$$

where $\boldsymbol{x}$ is the position vector to the center line of a fiber, ∇_X is the differential operator with respect to the reference (initial) frame, $\boldsymbol{S}$ is the second Piola-Kirchhoff stress, $\boldsymbol{F}$ is the deformation gradient tensor, and $\boldsymbol{F}_f$ is the interaction force from the fluid. As the aspect ratio of the fiber (a_s/h, see Fig. 2(b)) is small enough, the strain of a fiber is assumed to be small. Therefore $\boldsymbol{S}$ is calculated with Green-Lagrange strain $\boldsymbol{\epsilon}$:

$$\boldsymbol{S} = \boldsymbol{C} : \boldsymbol{\epsilon}, \tag{A2}$$

where $\boldsymbol{C}$ is the fourth-rank elasticity tensor. Even if fiber bends, we assume the cross section does not bend, and then, the components of $\boldsymbol{C}$ are given as follows:

$$C_{1111} = E, \tag{A3}$$

$$\begin{aligned} &C_{1212} = C_{1221} = C_{2121} = C_{2112} \\ &= C_{1313} = C_{1331} = C_{3131} = C_{3113} = k\frac{E}{2(1+\nu)}, \end{aligned} \tag{A4}$$

where E is Young's modulus, ν is the Poisson ratio, and k is a correction factor. According to Kubo and Noguchi (1995), the value of k is 5/6 when the shape of the cross section is rectangle. The other components of $\boldsymbol{C}$ are zero. Eq. (A1) is discretized with a finite element method.

A.3 Fluid-fiber interaction

Interaction between the fluid and fibers is calculated by the immersed boundary method proposed by Huang and Sung (2009). The interaction force $\boldsymbol{F}_f$ is given as

$$\boldsymbol{F}_f = -\kappa \left(\tilde{\boldsymbol{X}}_{IB}^{n+1} - 2{\boldsymbol{X}_{IB}}^n + {\boldsymbol{X}_{IB}}^{n-1} \right) , \tag{A5}$$

where

$$\tilde{\boldsymbol{X}}_{IB}^{n+1} = {\boldsymbol{X}_{IB}}^n + {\boldsymbol{U}_{IB}}^n \Delta t, \tag{A6}$$

$${\boldsymbol{U}_{IB}}^n(X,t) = \int_\Omega \boldsymbol{u}(x,t)\delta\left[\boldsymbol{X}(X,t) - \boldsymbol{x}\right] \mathrm{d}x, \tag{A7}$$

and Ω is the entire domain, δ is the discrete Dirac's delta function, κ is the penalty parameter of a sufficiently large value to impose no-slip condition (Kubo and Noguchi 1995). The force from fiber to the fluid is calculated by distributing $\boldsymbol{F}_f$ to the Eulerian frame:

$$\boldsymbol{f}_f = \int_\Gamma \boldsymbol{F}_f(\Gamma,t)\delta\left[\boldsymbol{x} - \boldsymbol{X}(\Gamma,t)\right] \mathrm{d}x, \tag{A8}$$

where Γ indicates the fiber surface.

The implementation of this immersed boundary method has been validated in Takeuchi et al. (2018).

B Longitudinal distributions of the x component of fluid velocity

Fig. B1 illustrates the longitudinal profiles of the x component of fluid velocity. It implies that interpolation of the fluid velocity u is a reasonable treatment, in particular, in deep inside the canopy.

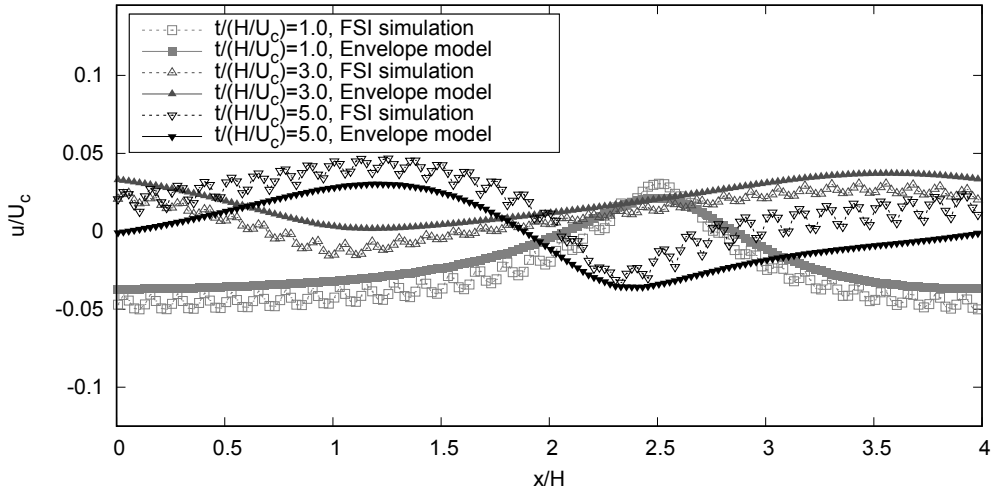

(a) $y/H = h/H$

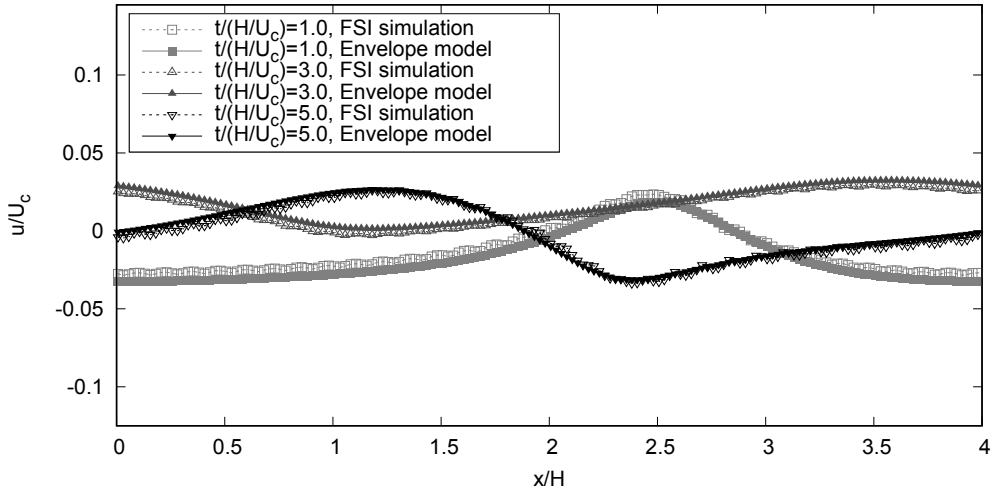

(b) $y/H = 0.35$

Figure B1: Longitudinal distributions of the x component of the fluid velocity at $t/(H/U_c) = 1.0, 3.0, 5.0$. The symbols are plotted at every 2 grid points in the x direction.

C Three dimensional model for uniform deformation

We investigate the conditions under which the envelope displacement model in three dimensions can be expressed in a similar form to that shown in the main body of the paper. In this section, we show an extension of the envelope model for uniform motion of the fibers.

The fibers are arranged at constant intervals (periodically) in both the x and z directions, and the direction normal to the wall is taken as y. The number density of the fibers is high, and the

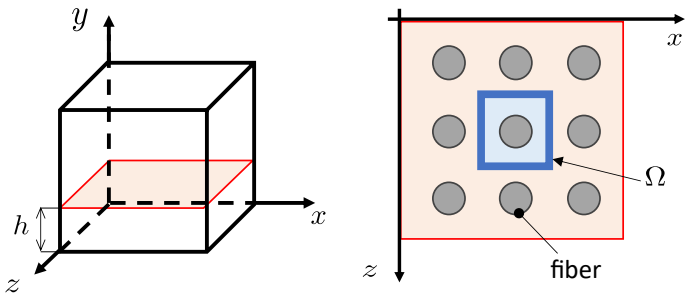

Figure C2: Schematic of the coordinate system in the three dimensional canopy flow and the unit region on the envelope.

fibers show small deflection. The flow is induced by constant pressure gradient $-\Delta p/\Delta x_i$ $(i = x, z)$. We also assume that the entire flow field is diffusion dominated.

A unit of the inter-fiber region Ω is considered, as schematically shown in Fig. C2, so that the flow fields and fiber deflections in the adjacent units are treated identically. The velocities of the fluid and the fiber in the unit region are assumed to follow each other closely, and the y component of the fluid velocity is set to zero inside the canopy.

Considering a plane average over Ω, an equation similar to Eq. (15) is obtained. Using the identical stress condition in the adjacent units, the moment of the fluid forces on a fiber in Ω is expressed in a similar form to Eq. (17), and finally, the time-evolving equation of the fiber displacement Z_i $(i = x, z)$ is given as follows:

$$\frac{\widetilde{\varrho}}{3}h^2\frac{\mathrm{d}^2 Z_i}{\mathrm{d}t^2} = -RC\frac{\mathrm{d}Z_i}{\mathrm{d}t} - \frac{\lambda_1^4}{3}\frac{EI}{Ah^2}Z_i - \frac{R}{2}h^2\frac{\Delta p}{\Delta x_i} + R\left(\boldsymbol{e}_i \cdot \langle\boldsymbol{\tau}\rangle_\Omega \cdot \boldsymbol{e}_y\right)h \ ,$$

where $\widetilde{\varrho} \overset{\text{def}}{=} \rho_s\Phi_s + R\rho_l\Phi_l$, $\Phi_k \overset{\text{def}}{=} A_k/A$ $(k = s, l)$ is the volume ratio of the region occupied by the fiber or fluid, $\langle\boldsymbol{\tau}\rangle_\Omega$ is the average shear stress in Ω, $\boldsymbol{e}_i$ is the basis vector, A is the area size of Ω at $y = h$, and the other symbols are the same as in Section 5.

The computational domain of the FSI simulation (L_x, H, L_z) is $(0.5, 1, 0.5)H$, respectively. The external pressure gradient $\Delta p/\Delta x(H/\rho_l u_\tau^2) = -1$ is induced in the x direction, where the friction velocity u_τ is the reference velocity in the absence of the canopy. The number of fibers is 8 in both the x and z directions (64 in total), and the inter-fiber distance a is uniformly $a/h = 1/6.4$ in both directions. In the simulation of the envelope model, the parameters are set to $R = 0.65$ and $C/(\rho_l u_\tau H) = 0.16$, and the other parameter values are the same as in Cases 1A and 1B.

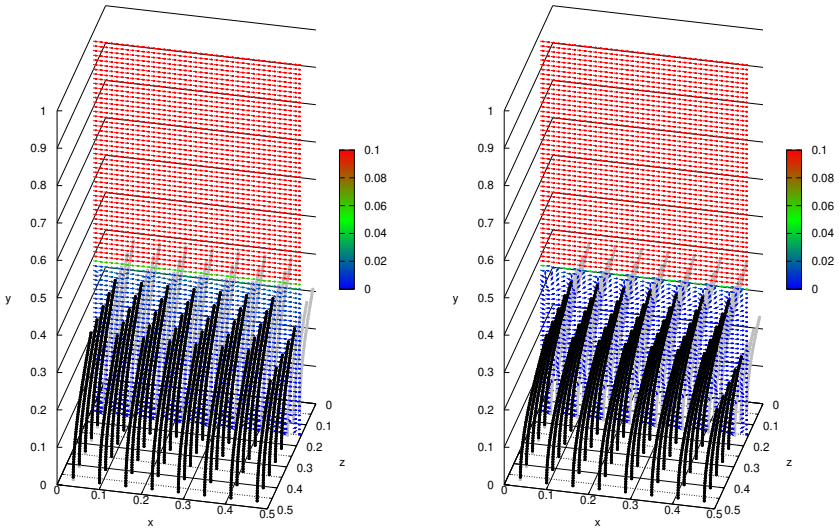

(a) $t/(H/u_\tau) = 1.0$ (b) $t/(H/u_\tau) = 4.0$

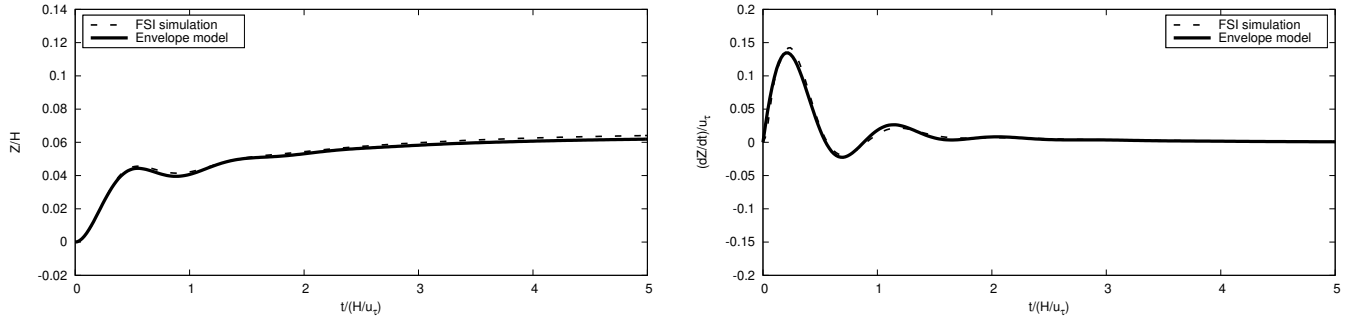

(c) Displacement (d) Tip velocity

Figure C3: Simulation result of three-dimensional canopy flow and time history of fiber deformation. (a)(b): Instantaneous flow fields of three-dimensional canopy flow obtained by the FSI simulation at different instances; transient state (a) and after reaching steady state (b). The fluid velocity vectors are colored based on the magnitude of the velocity. The fibers in front and behind the sliced plane are shown in black and grey, respectively. (c)(d): Time series of the x component of the displacement (c) and the tip velocity (d) of the envelope of the three-dimensional canopy. The solid lines show the results by our envelope model and the dashed lines are those of the FSI simulation.

Figs. C3(a) and (b) are the snapshots of instantaneous velocity fields and fibers obtained by the FSI simulation, and Figs. C3(c) and (d) compare the time histories of the tip displacements and tip velocities for the FSI (dashed line) and the present envelope model (solid line).

References

A. A. Amsden, and H. H. Harlow, A simplified MAC technique for incompressible fluid flow calculations, Journal of Computational Physics 6.2, 322-325,(1970).

J. R. Blake, A spherical envelope approach to ciliary propulsion, Journal of Fluid Mechanics 46(1), 199-208, (1971).

V. B. L. Boppana, Z. -T. Xie, and I. P. Castro, Thermal stratification effects on flow over a generic urban canopy, Boundary-Layer Meteorology 153, 141-162, (2014).

S. Chateau, J. Favier, U. D'ortona, S. Poncet, Transport efficiency of metachronal waves in 3D cilium arrays immersed in a two-phase flow, Journal of Fluid Mechanics 824, 931-961, (2017).

H. Chen, Q. P. Zou, Eulerian–Lagrangian flow-vegetation interaction model using immersed boundary method and OpenFOAM, Advances in Water Resources, 126, 176-192, (2019).

J. Finnigan, Turbulence in waving wheat, Boundary-Layer Meteorology 16, 181–211, (1979).

J. Finnigan, Turbulence in plant canopies, Annual Review of Fluid Mechanics 32.1 , 519-571, (2000).

J. Elgeti, G. Gompper, Emergence of metachronal waves in cilia arrays, PNAS 110(12), 4470-4475, (2013).

G. R. Fulford, J. R. Blake, Muco-ciliary transport in the lung, Journal of Theoretical Biology 121(4), 381-402

W. Gao, R. H. Shaw, K. T. Paw U, Observation of organized structure in turbulent flow within and above a forest canopy, Boundary Layer Studies and Applications: A Special Issue of Boundary-Layer Meteorology in honor of Dr. Hans A. Panofsky, 349–377, (1989).

A. Gopinath, L. Mahadevan, Elastohydrodynamics of wet bristles, carpets and brushes, Proceedings Of The Royal Society A: Mathematical, Physical and Engineering Sciences 467(2130), 1665-1685, (2011).

W. X. Huang, H. J. Sung, An immersed boundary method for fluid–flexible structure interaction, Computer Methods in Applied Mechanics and Engineering 198(33-36), 2650-2661, (2009).

M. Kanda, M. Hino, Organized structures in developing turbulent flow within and above a plant canopy, using a large eddy simulation, Boundary-Layer Meteorology 68.3, 237-257, (1994).

S. N. Khaderi, J. M. den Toonder, P. R. Onck, Magnetic artificial cilia for microfluidic propulsion, Advances in Applied Mechanics 48, 1-78, (2015).

A. S. Khair, N. G. Chisholm, Expansions at small Reynolds numbers for the locomotion of a spherical squirmer, Physics of Fluids, 26(1), (2014).

T. Kubo, H. Noguchi, Fundamentals and Applications of Nonlinear Finite Element Method, Maruzen Publishing Co., Ltd., (1995).

Q. Li, Z. H. Wang, Large-eddy simulation of the impact of urban trees on momentum and heat fluxes, Agricultural and Forest Meteorology 255: 44-56, (2018).

M. J. Lighthill, On the squirming motion of nearly spherical deformable bodies through liquids at very small Reynolds numbers, Communications on Pure and Applied Mathematics 5(2), 109-118, (1952).

F. Meng, R. R. Bennett, N. Uchida, R. Golestanian, Conditions for metachronal coordination in arrays of model cilia, Proceedings of the National Academy of Sciences 118(32), e2102828118, (2021).

E. Milana, R. Zhang, M. R. Vetrano, S. Peerlinck, M. D. Volder, P. R. Onck, B. Gorissen, Metachronal patterns in artificial cilia for low Reynolds number fluid propulsion, Science Advances 6(49), eabd2508, (2020).

A. Monti, M. Omidyeganeh, B. Eckhardt, A. Pinelli, On the genesis of different regimes in canopy flows: a numerical investigation, Journal of Fluid Mechanics, 891, A9, (2020).

M. H. Nepf, Flow and transport in regions with aquatic vegetation, Annual Review of Fluid Mechanics 44.1: 123-142, (2012).

C. L. V. Oosten, C. W. M. Bastiaansen, D. J. Broer, Printed artificial cilia from liquid-crystal network actuators modularly driven by light, Nature Materials 8, 677–682, (2009).

M. R. Raupach, P. A. Coppin, B. J. Legg, Experiments on scalar dispersion within a model plant canopy part I: The turbulence structure, Boundary-Layer Meteorology 35, 21–52, (1986)

T. W. Secomb, R. Hsu, A. R. Pries, A model for red blood cell motion in glycocalyx-lined capillaries, American Journal of Physiology-Heart and Circulatory Physiology 274(3), H1016-H1022, (1998).

S. A. Mattis, C. N. Dawson, C. E. Kees, M. W. Farthing, An immersed structure approach for fluid-vegetation interaction, Advances in Water Resources 80 : 1-16, (2015).

T. Stoesser, G. P. Salvador, W. Rodi, P. Diplas, Large eddy simulation of turbulent flow through submerged vegetation, Transport in Porous Media 78 : 347-365, (2009).

S. Takeuchi, H. Fukuoka, J. Gu, T. Kajishima, Interaction problem between fluid and membrane by a consistent direct discretisation approach, Journal of Computational Physics 371, pp.1018–1042 (2018)

A. E. Tilley, M. S. Walters, R. Shaykhiev, R. G. Crystal, Cilia Dysfunction in Lung Disease, Annual Review of Physiology 77, 379-406, (2015).

N. Uchida, R. Golestanian, Synchronization and Collective Dynamics in a Carpet of Microfluidic Rotors, Physical Review Letters 104.17, 178103, (2010).

M. Vilfan, A. Potočnik, B. Kavčič, N. Osterman, I. Poberaj, A. Vilfan, D. Babič, Self-assembled artificial cilia, Proceedings of the National Academy of Sciences 107(5), 1844-1847, (2010).

S. Wang, A. Ardekani, Inertial squirmer, Physics of Fluids 24.10, (2012).

W. Wang, Q. Liu, I. Tanasijevic, M. F. Reynolds, A. J. Cortese, M. Z. Miskin, M. C. Cao, D. A. Muller, A. C. Molnar, E. Lauga, P. L. McEuen, I. Cohen, Cilia metasurfaces for electronically programmable microfluidic manipulation, Nature 605, 681-686, (2022).

J. T. Zhang, X. H. Su, Numerical model for flow motion with vegetation, Journal of Hydrodynamics 20(2), 172-178, (2008).

R. Zhang, J. d. Toonder, P. R. Onck, Transport and mixing by metachronal waves in nonreciprocal soft robotic pneumatic artificial cilia at low Reynolds numbers, Physics of Fluids 33(9), (2021).

Acknowledgements

This work is partly supported by Grants-in-Aid for Scientific Research (B) No. JP23K26039 of the Japan Society for the Promotion of Science (JSPS).

Author contributions

S.A. developed the mathematical model and conducted data mining. K.O. contributed to the core design of the numerical code, and S.T. worked for conceptualization and validation. Both S.A. and S.T. wrote the manuscript, and K.O. reviewed the manuscript.

Declarations

Conflict of interest The authors declare that they have no conflict of interest.